DESIGN OF INTELLIGENT INTERNET OF THINGS AND INTERNET OF BODIES SENSOR NODES

by

Shitij Avlani

A Thesis

Submitted to the Faculty of Purdue University

In Partial Fulfillment of the Requirements for the degree of

Master of Science in Electrical and Computer Engineering

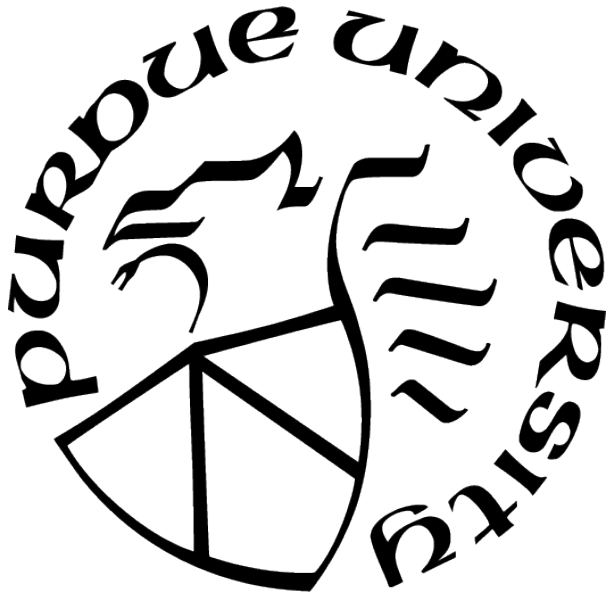

School of Electrical and Computer Engineering

West Lafayette, Indiana

August 2021

THE PURDUE UNIVERSITY GRADUATE SCHOOL
STATEMENT OF COMMITTEE APPROVAL

Dr. Shreyas Sen, Chair

School of Electrical and Computer Engineering

Dr. Byunghoo Jung

School of Electrical and Computer Engineering

Dr. Kaushik Roy

School of Electrical and Computer Engineering

Approved by:

Dr. Dimitrios Peroulis

To my parents *Archana* and *Tushar*, who have been the greatest source of inspiration, encouragement, and support in my life

ACKNOWLEDGMENTS

First and foremost I am extremely grateful to my supervisor, Prof. Shreyas Sen for his invaluable advice, support, and patience during my master's study. I would like to thank all the members in the SPARC Lab research group for their kind help and support. Finally, I would like to express my gratitude to my family and friends. Without their tremendous understanding and encouragement in the past few years, it would be impossible for me to complete my study.

TABLE OF CONTENTS

LIST OF TABLES

LIST OF FIGURES

ABSTRACT

Energy-efficient communication has remained the primary bottleneck in achieving fully energy-autonomous IoT nodes. Several scenarios including In-Sensor-Analytics (ISA), Collaborative Intelligence (CI) and Context-Aware-Switching (CAS) of the cluster-head during CI have been explored to trade-off the energies required for communication and computation in a wireless sensor network deployed in a mesh for multi-sensor measurement. A real-time co-optimization algorithm was developed for minimizing the energy consumption in the network for maximizing the overall battery lifetime of individual nodes.

The difficulty of achieving the design goals of lifetime, information accuracy, transmission distance, and cost, using traditional battery powered devices has driven significant research in energy-harvested wireless sensor nodes. This challenge is further amplified by the inherent power intensive nature of long-range communication when sensor networks are required to span vast areas such as agricultural fields and remote terrain. Solar power is a common energy source is wireless sensor nodes, however, it is not reliable due to fluctuations in power stemming from the changing seasons and weather conditions. This paper tackles these issues by presenting a perpetually-powered, energy-harvesting sensor node which utilizes a minimally sized solar cell and is capable of long range communication by dynamically co-optimizing energy consumption and information transfer, termed as Energy-Information Dynamic Co-Optimization (EICO). This energy-information intelligence is achieved by adaptive duty cycling of information transfer based on the total amount of energy available from the harvester and charge storage element to optimize the energy consumption of the sensor node, while employing event driven communication to minimize loss of information. We show results of continuous monitoring across 1Km without replacing the battery and maintaining an information accuracy of at least 95%.

Decades of continuous scaling in semiconductor technology has resulted in a drastic reduction in the cost and size of unit computing. This has enabled the design and development of small form factor wearable devices which communicate with each other to form a network around the body, commonly known as the Wireless Body Area Network (WBAN). These devices have found significant application for medical purposes such as reading surface bio-

potential signals for monitoring, diagnosis, and therapy. One such device for the management of oropharyngeal swallowing disorders is described in this thesis. Radio wave transmission over air is the commonly used method of communication among these devices, but in recent years Human Body Communication has shown great promise to replace wireless communication for information exchange in a WBAN. However, there are very few studies in literature, that systematically study the channel loss of capacitive HBC for *wearable devices* over a wide frequency range with different terminations at the receiver, partly due to the need for *miniaturized wearable devices* for an accurate study. This thesis also measures and explores the channel loss of capacitive HBC from 100KHz to 1GHz for both high-impedance and 50Ω terminations using wearable, battery powered devices; which is mandatory for accurate measurement of the HBC channel-loss, due to ground coupling effects. The measured results provide a consistent wearable, wide-frequency HBC channel loss data and could serve as a backbone for the emerging field of HBC by aiding in the selection of an appropriate operation frequency and termination.

Lastly, the power and security benefits of human body communication is demonstrated by extending it to animals (animal body communication). A sub-inch^3, custom-designed sensor node is built using off the shelf components which is capable of sensing and transmitting biopotential signals, through the body of the rat at significantly lower powers compared to traditional wireless transmissions. In-vivo experimental analysis proves that ABC successfully transmits acquired electrocardiogram (EKG) signals through the body with correlation accuracy >99% when compared to traditional wireless communication modalities, with a 50x reduction in power consumption.

1. INTRODUCTION

Advances in semiconductor technology in the last couple of decades has enabled the proliferation of smart connected devices, collectively referred to as The Internet of Things. They have found such abundant application in all spheres of life, from smart homes and cities, wearable and implantable medical devices to agriculture and vehicles, that CISCO predicts by the year 2022 there will be machine-to-machine (M2M) communication between 14.2 billion connected devices [1]. Low-power and cheap computing elements have enabled these devices to provide complex in-situ processing capabilities in a small and energy efficient form factor. However, a significant percentage of these devices are battery powered and require regular replacements which is bound to create a profound environmental impact, not to mention the time and cost of human intervention. This thesis aims to address this problem by reducing the energy consumption of wearable devices and enabling energy harvesting in an energy intelligent fashion for other battery-powered, wireless, connected devices.

The first, refers to small form factor devices that reside on or around the body and communicate with each other, which is referred to as a Body Area Network. These devices conventionally communicate using radio-frequency signals which can be extremely power intensive and affect the lifetime, size and cost of the device. By exploiting the electrical characteristics of the human body, a form communication can be established which has the mobility and benefits of wireless communication at the power consumption of wire-line communication, which is approximately 10,000X lower. This thesis builds the first accurate termination dependent channel model from 100KHz to 1GHz of the human body for wearable devices, to further optimize the design of these communication systems. Also, human body communication is extended to animals by describing a custom-designed wearable sensor node for capturing bio-potential signals and transmitting that data through the animal's body, thereby demonstrating the energy benefit of this communication modality.

The second scenario pertains to all other M2M connected devices, such as those for agriculture, industrial, or environmental monitoring where batteries are utilized and the finite lifetime of these devices risks the temporary loss of information while adding the cost of spending time and money to either replace the battery or place new sensor nodes.

This can be subverted by making the devices energy harvested, however, there are few such implementations since the instantaneous power generated by energy harvesters is not sufficient for powering long range communication systems without duty cycling of information and using large, bulky energy harvesters. This thesis proposes an energy aware system which addresses this issue by optimizing the energy consumption of the sensor node by varying the transmission rate of information based on the total amount of energy available (harvested and stored), while minimizing the loss of information through event driven communication. Obviously this can also be extended to wearable devices by making an appropriate choice for the harvesting element.

Chapter 2 explores the design of intelligent Internet of Things sensor nodes. It briefly describes the methods that can be used to reduce the power consumption of battery powered wireless sensor nodes in a mesh network to increase its overall lifetime and thereby lays out the groundwork and need for an energy-harvested long-range sensor node. The chapter then dwells in detail on the design challenges and constraints to make long-range wireless sensor nodes perpetually powered, and proposes a solution in the from of Energy information Dynamic Co-optimization (EICO) which makes the sensor node energy intelligent by varying the data transmission rate based on the total amount of energy available while using anomaly detection to transmit data to prevent information loss.

Chapter 3 discusses the design of internet of body devices starting with a wearable device that collects data from a flexible submental sensor patch for management of oropharyngeal swallowing disorders. This device transmits data over radio-frequency signals which are energy intensive. Human Body communication is introduced as a more secure, energy efficient way to transmit data and the first termination dependent channel model from 100KHz to 1GHz is described in section 2. Finally, human body communication is extended to animals as a wearable device to collect bio-physical signals and simultaneously transmit data through body-wire communication, which is proven to be as reliable as Bluetooth.

2. DESIGN OF INTERNET OF THINGS SENSOR NODES

Most of the content in this chapter has been extracted verbatim from the papers:

S. Avlani et al. "Energy Harvesting Long-Range Sensor Nodes Using In-Sensor-Analytics and Energy Intelligence" to be submitted to IEEE Journal of Internet of Things.

B. Chatterjee et al., "Context-Aware Collaborative Intelligence With Spatio-Temporal In-Sensor-Analytics for Efficient Communication in a Large-Area IoT Testbed," in IEEE Internet of Things Journal, vol. 8, no. 8, pp. 6800-6814, 15 April15, 2021, doi: 10.1109/JIOT.2020.3036087.

2.1 Context-Aware Collaborative Intelligence With Spatio-Temporal In-Sensor-Analytics for Efficient Communication in a Large-Area IoT Testbed

2.1.1 Introduction

Decades of continuous scaling has reduced the energy of unit computing to virtually zero, while energy-efficient communication has remained the primary bottleneck in achieving fully energy-autonomous IoT nodes. This paper presents and analyzes the trade-offs between the energies required for communication and computation in a wireless sensor network, deployed in a mesh architecture over a 2400-acre university campus, and is targeted towards multi-sensor measurement of temperature, humidity and water nitrate concentration for smart agriculture. Several scenarios involving In-Sensor-Analytics (ISA), Collaborative Intelligence (CI) and Context-Aware-Switching (CAS) of the cluster-head during CI has been considered. A real-time co-optimization algorithm has been developed for minimizing the energy consumption in the network, hence maximizing the overall battery lifetime of individual nodes. Measurement results show that the proposed ISA consumes ≈467X lower energy as compared to traditional Bluetooth Low Energy (BLE) communication, and ≈69,500X lower energy as compared with Long Range (LoRa) communication. When the ISA is implemented in conjunction with LoRa, the lifetime of the node increases from a mere 4.3 hours to 66.6 days with a 230 mAh coin cell battery, while preserving more than 98% of the total information. The CI and CAS algorithms help in extending the worst-case node lifetime by an additional 50%, thereby exhibiting an overall network lifetime of ≈104 days, which is >90% of the theoretical limits as posed by the leakage currents present in the system,

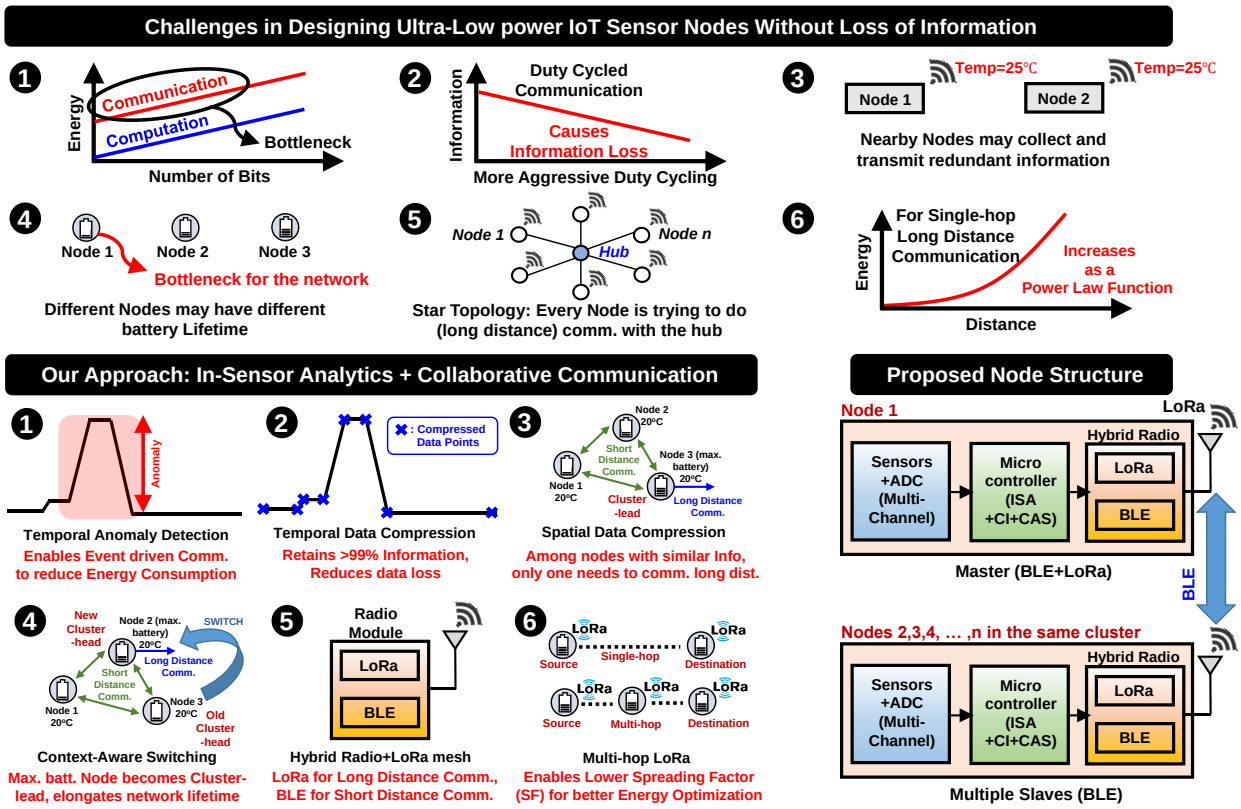

Figure 2.1. The six challenges identified in designing ultra-low power IoT sensor node and our proposed solution, addressing all six challenges. The salient features of the implemented sensor node with In-Sensor Analytics (ISA) and Collaborative Intelligence (CI) are also described in brief: 1. Temporal Anomaly Detection, 2. Temporal Data Compression, 3. Spatial Data Compression/CI, 4. Context-Aware switching (CAS), 5. Hybrid Radio, 6. Multi-hop LoRa

while effectively transferring information sampled every second. A web-based monitoring system was developed to archive the measured data in a continuous manner, and to report anomalies in the measured data.

2.1.2 In-Sensor Analytics

During normal operation the sensor duty cycles the transmission of data at a very slow rate. To prevent the loss of meaningful information in-sensor analytics for anomaly detection is incorporated, the basics of which is depicted in Fig. 2.2. A threshold ($x\%$) is defined for each of the sensed variables, which was previously calculated by analyzing the data collected

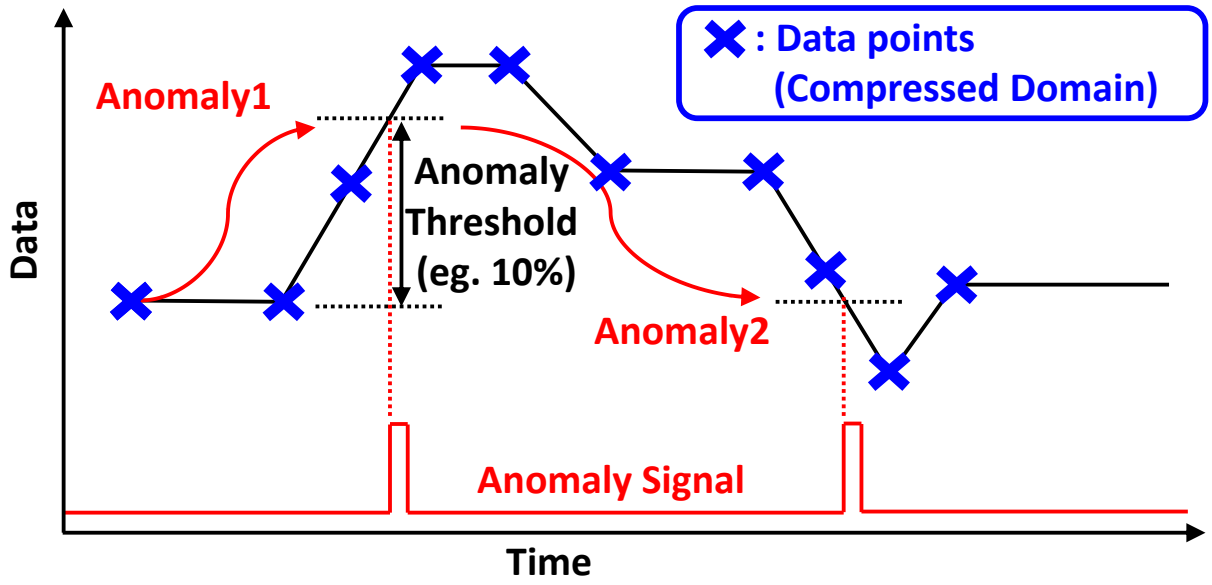

Figure 2.2. Illustration of Anomaly Detection and Data Compression.

over a span of more than 4 weeks using a K-means clustering algorithm. when the difference in standard deviation between the data sampled at real time and its moving average is greater than the above defined threshold, an anomaly event is generated which triggers the communication of sampled data. A provision is maintained to alter these thresholds when required.

For example, when the threshold for anomaly detection is defined as 10% and 100 samples of uncompressed data is collected in 100 seconds, only 12 data points are transmitted by the temporal data compression algorithm (compression ratio = 100/12 = 8.33). Of these 12 data points, 10 are transmitted due to an anomaly in the sensor readings. Some of those 10 data points are also transmitted while the sensor readings gradually reduces back to its original value. In the absence of this artificially created anomaly, the compression rate would be much higher. The correlation coefficient between the compressed, and uncompressed data is greater than 98%

Fig. 2.3 shows the data from two devices, Device-19 functions without in-sensor analytics, while Device-20 incorporates in-sensor analytics. The two devices are placed beside each other in a lab setting. A custom built device that automatically generated environmental

```
Data: Samples from environmental sensors
Result: Anomalies detected in sampled data
Initialize the threshold (x) of the k-means clustering algorithm;
while New sample available do
    if data >= x% or <= x% from last anomaly (ISA) then
        activate sub-GHz communication;
        send temporally compressed data stream to the receiver;
        record new transmission time; deactivate sub-GHz communication;
    else
        wait for the next anomaly/next transmission time;
        stay in low-power sense and compute mode;
    end
    if time since last transmission = transmission interval then
        activate sub-GHz communication;
        send current data point to the receiver;
        record new transmission time; deactivate sub-GHz communication;
    else
        wait for the next anomaly/next transmission time;
        stay in low-power sense and compute mode;
    end
end
```

Algorithm 1: Anomaly Detection followed by data transmission using Long Range communication

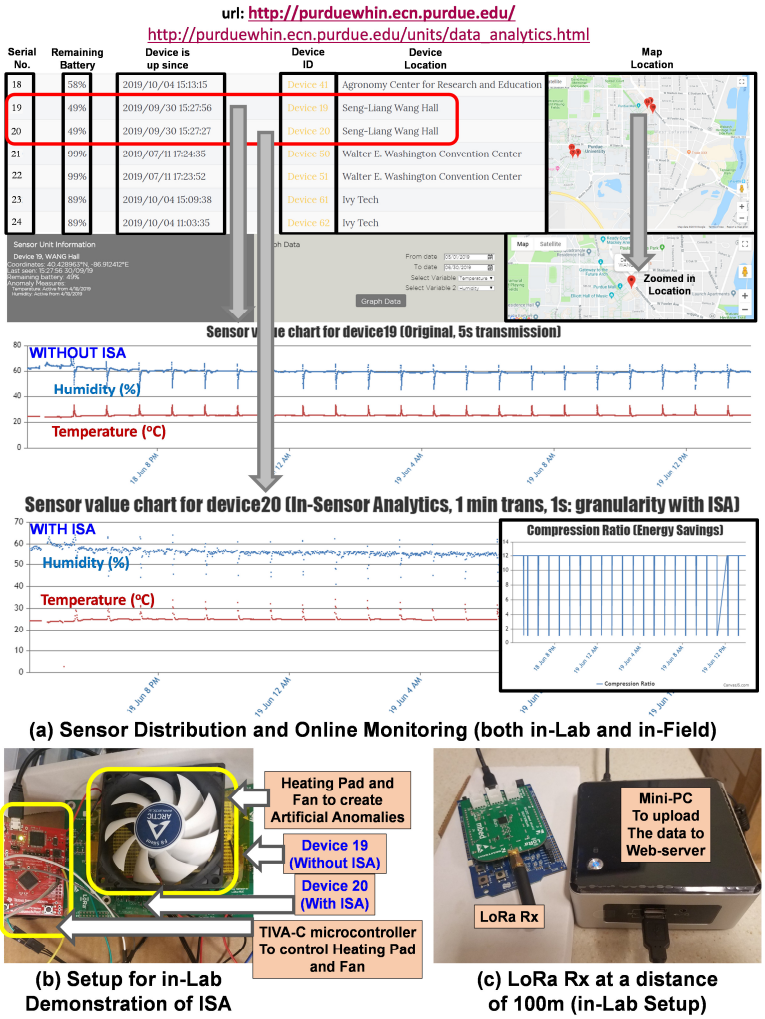

Figure 2.3. (a) Sensor distribution and live monitoring as performed in https://purduewhin.ecn.purdue.edu/. Device 19 (without ISA) and Device 20 (with ISA) are placed on the same location, $<$ 1 foot away from each other. Both Device 19 and device 20 samples once every 5 seconds. Device 19 transmits the data when it is sampled, while Device 20 compresses the data and sends out when there is an anomaly, which is artificially created every minute using a heating pad and cooling fan for demonstration purpose. This demonstration achieves energy savings of $\approx$12X, simply due to the ratios of transmission time (website link); (b) Setup for in-Lab demonstration of ISA with Device 19 and Device 20; (c) LoRa Rx at a distance of 100 m (in-Lab Setup).

anomalies was used compare the readings received from both devices. Temperature and humidity anomalies were artificially created through a heating pad and cooling fan placed

right on top of the sensors. These transducers were controlled by Tiva-C series microcontroller (Texas Instruments) through a couple of relays. The anomaly pattern repeated every 60 minutes, wherein the heating pad was turned on for 1 minute following which the cooling fan operated for 5 minutes. Device 20 transmitted compressed data once every minute and at the occurrence of an anomaly, while device 19 transmitted uncompressed data at a 5 second interval. This demonstration showcases an energy savings of approximately 12X for Device-20 at a correlation coefficient > 0.98, due to the ratio of transmission interval (https://purduewhin.ecn.purdue.edu/data_analytics/).

2.2 EICO: Energy-Harvesting Long-Range Environmental Sensor Nodes with Energy-Information Dynamic Co-Optimization

2.2.1 Introduction

A long-range wireless sensor node is primarily used in smart cities and smart agricultural fields, and has multiple design variables ranging from the choice of transducers, power supply, communication and in-built computation capabilities, to cost, size, and network protocols. Batteries are typically the choice of power source for sensor nodes deployed in remote locations, large areas where the cost of wiring would be unfeasible, or for mobility, such as agricultural fields, habitat and environment monitoring [2], volcano monitoring [3], and structural monitoring [4] to name a few. This creates a major limitation of finite battery capacity, resulting in a finite lifetime which adds an overhead of spending time and money to either replace the battery or place new sensor nodes while risking temporary loss of information. Designers could opt for larger batteries at the cost of increasing the size, weight and price of the device.

This has naturally sparked an increasing interest in energy harvesting sensor nodes since they can operate for many years at a time without requiring human intervention to replace the battery or the node itself. However, there are few such implementations since the instantaneous power generated by energy harvesters is not always sufficient for powering long range communication systems and commercially available sensor nodes can be extremely power hungry. Some designs either use solar panels to meet this power requirement, which can be prohibitively expensive and large, or create low power systems that duty cycle data transmission such that information is lost in the process. Hence, its evident that there is an inconsistency between the power available from energy harvesters and the power consumed by wireless sensor nodes to perform the required task without compromising on the information reported. This motivates the creation of an energy harvesting sensor node capable of long range communication using a cheap and small energy source by optimizing its power consumption to function within the bounds of the energy harvester, without losing any information in the process.

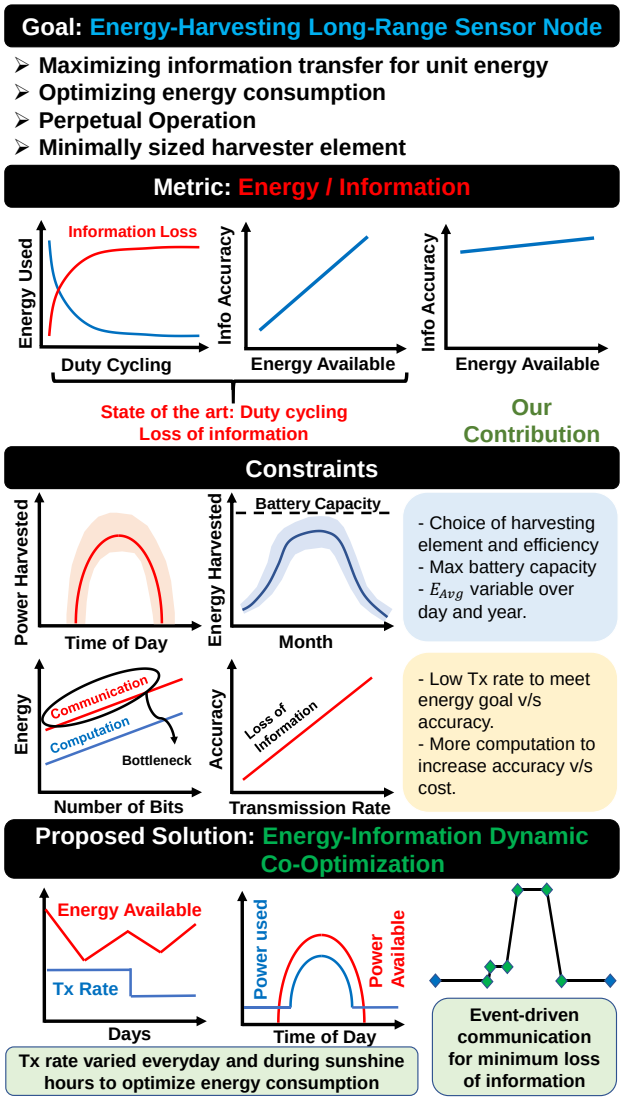

Figure 2.4. The performance of state of the art energy-harvested long-range wireless sensor nodes is introduced in terms of an Energy/Information metric and the constraints to improve this metric are depicted. Finally, our proposed solution to optimize this metric using EICO is illustrated.

A multitude of software techniques have been proposed to prolong the lifetime of battery powered wireless sensor nodes without any energy harvesting modalities. Some of these methods include energy-aware network protocols, duty-cycling strategies, redundant placement of nodes, and various in-sensor analytics [5], [6]. A prominent example is an IoT device developed by Intel which implemented multiple energy-scavenging techniques like duty cycling to reduce the overall average power, however, duty cycling reduced the overall on-time

[7]. These methods will prolong the time between battery replacements but still require human intervention, often at the cost of information loss, sensing reliability, and increased costs due larger quantity of nodes from an increased number of hops.

Extensive research has been performed to address this problem by utilizing renewable energy through energy harvesters to power wireless sensor nodes. Some of the prominent energy sources include photovoltaics, thermoelectric generators, wind energy, piezoelectic, radio-frequency based methods, etc. [8]. Due to the low power output of these sources ($15\mu W - 30mW$ per cm under perfect conditions), most of the implementations in literature are only able to meet the needs of low-energy, short-range communication and often have low reporting intervals with loss of information. Long-range communication is extremely power intensive (150-300mW) which creates a large power discrepancy. Lee, et.al.[9], attempted to address this by proposing a floating, energy-harvested, long-range sensor node which combined solar and thermoelectric energy harvesting, but the power consumption was 6.6216 Wh/day (275.9mW) and required large solar panels to meet this demand which made the device excessively large and expensive. Stamenkovic, et.al. [10], was able to shrink the size of the energy source to $40.7cm^2$ by optimizing the design using hybrid energy modelling but paid the price in information loss since data was transmitted at maximum rate of once every minute. This clearly shows that there is a discrepancy between the availability of energy from a reasonably sized energy source and the energy required to perform long range communication with minimal loss of information.

Various methods have been explored to increase the power harvested in wireless sensor nodes by introducing a power management module to reduce the mismatch between the power harvested and the power consumed by the sensor node. These include nonlinear techniques for piezoelectric and electromagnetic energy harvesters by toggling switches at the appropriate time to form an LC oscillator using an inductor or capacitor [11] and resistive or impedance matching for maximum power transfer in energy harvesters using either a photovoltaic, thermoelectric, or piezoelectric sources [12], [13]. [14] proposed a combined power management module with an energy aware program to deal with the power mismatch by managing the energy flow from the storage capacitor. [15] proposed a solar prediction algorithm to exploit solar energy more efficiently by taking into account both the current

and past-days weather conditions, however, it requires a DSP and has significant difficulties during variable weather conditions.

To the best of our knowledge, there is no literature available on creating an energy aware system which addresses this issue by optimizing the power consumption of the sensor node by varying the transmission rate of information based on the total amount of energy available (harvested and stored), while minimizing the loss of information through event driven communication. We term this as "Energy-Information Dynamic Co-Optimization (EICO)", which has been presented in this paper.

Table 2.1. Variables for Energy-Information Dynamic Co-Optimization

Variable	Description
$Tx_{minRate}$	Minimum data transmission rate
E_{BATT}	Energy currently stored in battery
E_{buf}	Critical (buffer) energy level
D_{max}	Lifetime (days) without energy harvested
E_{avail}	Energy harvested on previous day

In this work, we have proposed an embedded hardware architecture and software strategies to create a perpetually powered, energy-harvested, long-range sensor node using in-sensor analytics and energy-aware data transmission. In-sensor analytics enables the detection of anomalies by event-driven communication and temporally compresses data with a maximum of 5% loss of information. Energy-aware data transmission measures the total energy available from the energy harvester on a given day and the state of the charge storage device to vary the data transmission rate of the wireless sensor node, thereby optimizing the transfer of information to the energy consumed by the device. A brief description of the important variables involved to enable this is shown in Table 2.1, with a pictorial depiction in Fig.2.4. A proprietary sub-GHz transceiver from Texas Instruments [16] was chosen over LoRa, SigFox, and NB-IoT for long range communication since it has the best receiver sensitivity, encryption features, and provides a sufficient range (at least 1-5 Km). Additionally, it allows for the development of private networks by using the unlicensed 915MHz ISM band in Region-2 of the International Telecommunication Union.

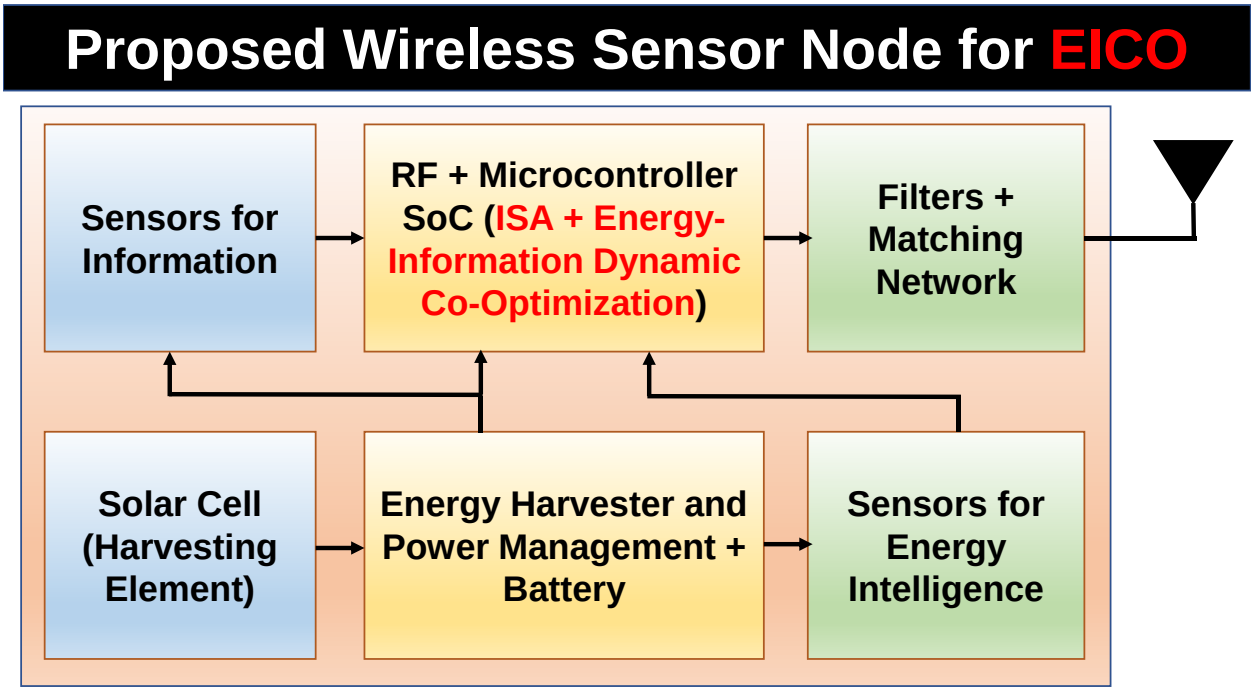

Figure 2.5. Block diagram of the proposed energy-harvested, long-range communication wireless sensor ndoe.

Fig. 2.5 shows the top-level hardware architecture of the proposed custom-built IOT sensor node. Digital sensors for temperature, humidity, and light intensity (lux) are used as the environmental sensors for information and a solar cell is used as the source for the energy harvester for demonstration purposes. The microcontroller SoC applies the in-sensor analytics algorithm to the the discretized and quantized values read from the sensors to detect anomalies and initiate communication when the difference between the values crosses a predefined threshold of variance. During the absence of anomalies, the sensor node duty cycles the data transmission rate which is calculated from the total energy harvested on the previous day and the energy stored in the battery, such that the device can function for at least 14 (D_{max}) days if the harvester were to fail. This will optimize the energy consumption of the device to maximize the transfer of information and improve accuracy, while ensuring that the device remains perpetually powered.

2.2.2 Theoretical Analysis

Limitations of Energy Harvesting

Advances in semiconductor technology over the years has dramatically increased the efficiency and output power of energy harvesting systems, while opening new avenues of energy sources like thermo-electric generators (TEG) and targeted radio frequency (RF) sources. TEGs can generate between 20 μW to 10mW of power per cm^2 of area based on the temperature gradient. Output power from RF sources is largely limited to the 10 μW - a few 100 μWs range and requires high power RF sources in close proximity. Photo-voltaic cells produce an output power ranging from 100 μW - 200mW based on their construction, dimensions, spectrum of operation and light intensity. TEG and RF sources would be more suitable for devices placed in industrial locations and wearable devices, whereas photovoltaics would find better use in outdoor applications. A summary of these energy sources is shown in Table 2.2 for unit length under specific conditions.

Table 2.2. Unit power of energy sources [17] [18] [19]

Source	Power	Parameter
RF	$15\mu W$	Multiband Receiver (RF: $1mW/cm^2$)
TEG	$20.53\mu W/cm$	Ag/Ni Thermocouple (ΔT=127 C)
Photovoltaic	$28mW/cm^2$	Si-Crystalline ($1KW/m^2$ solar radiation)
Piezoelectric	$19mW/cm^2$	-

The power intensive nature of long range communication and limited power availability warrants the need for low power architectures, careful selection of energy sources, and planning of the power budget. The sensor node proposed in this paper is primarily built for monitoring environmental variables with applications in agricultural fields or climate studies and would be placed outdoors in open fields, making solar power the obvious choice.

The sensor nodes will be deployed in Indiana, which has approximately 3.5 times lower average solar insolation in winter as compared to the summer months which is illustrated in Fig. 2.6. The energy harvesting system and consequently the sensor node needs to be able to operate by adapting to the lower energy limit, thereby selecting that as the design

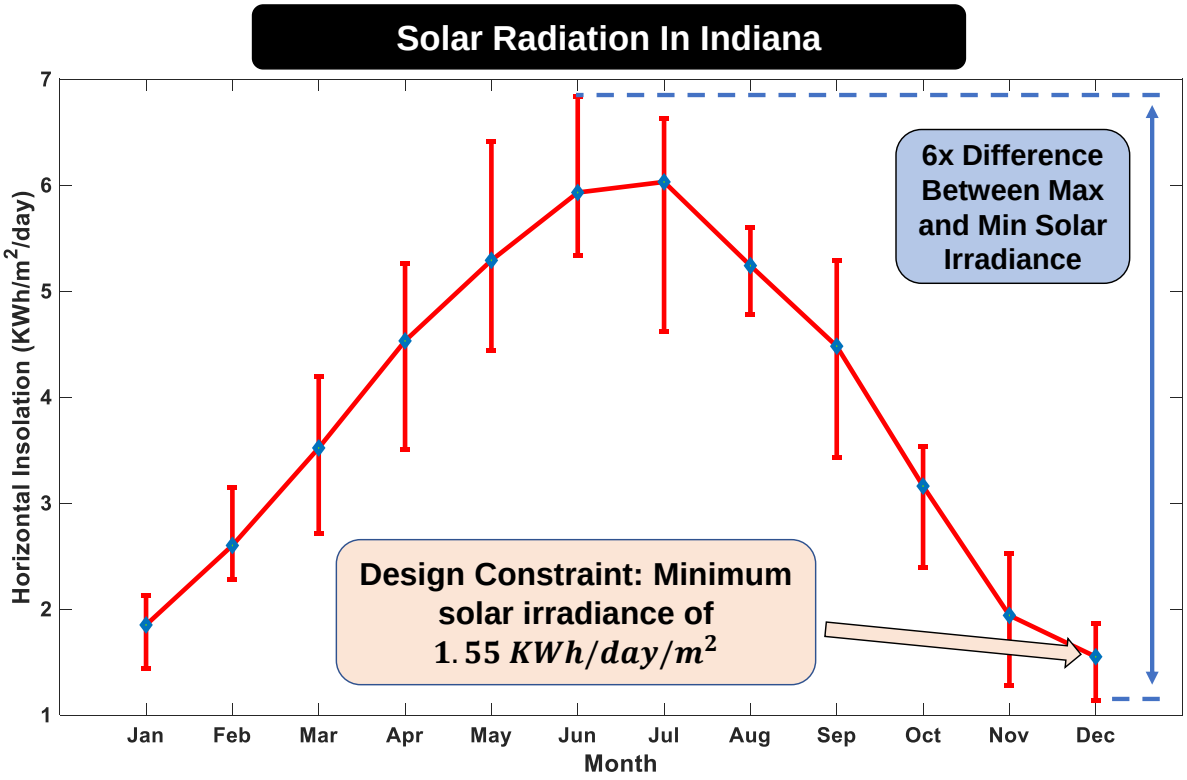

Figure 2.6. Maximum, minimum, and average solar insolation received on an average day during a given month in Indiana which serves as the design constraint for power consumption. [20]

constraint. Minimum solar insolation is in the month of December, when an average of $1.55 KWh/m^2/day$ is received. The theoretical power harvested is then calculated as shown in Eq. (2.1).

$$P_{Harvested} = P_{rad} \times \text{Area of Solar Cell} \times \frac{\eta}{24} \tag{2.1}$$

Where, P_{rad} is the average solar power irradiated and η is the efficiency of the cell. Assuming a dimension of $30cm^2$ and a conservative efficiency of $10\%(\eta)$, the theoretical power consumption limit is calculated to be 2.01mW or 173.9J of energy per day. The design constraint for minimum power consumption was set at 60% of 2.01mW, i.e. 1.20mW or 105J per day in order to to account for losses in the power management system and producing surplus energy to try and recharge the charge storage device if it is at its critical threshold.

Theoretical Limits of Computation and Communication Energy

Representing the energy per bit for computation and communication to be $E_{cmp,u}$ and $E_{com,u}$, respectively, the total energy consumed in a system for computation (E_{cmp}) and communication (E_{com}) is written as

$$\begin{aligned} E_{cmp} &= (E_{cmp,u}) \times \text{No. of bits switched} \\ E_{com} &= (E_{com,u}) \times \text{No. of bits transmitted} \end{aligned} \tag{2.2}$$

Energy consumed during computation primarily comprises of digital calculations. Therefore, it can be approximated as the dynamic energy at a frequency of operation beyond the leakage-dominant region, given by $(E_{cmp,u}) = CV^2$ [21]. In an ideal technology that allows for zero device capacitance, $(E_{cmp,u})$ reduces to its theoretical limit given by Landauer's principle [22]. Eq. (2.3) illustrates this, where κ is Boltzmann constant and T is the absolute temperature. This translates to an $(E_{cmp,u})_{th\_min}$ of 2.85×10^{-21} J/bit at room temperatures (T=298K).

$$(E_{cmp,u})_{th\_min} = \kappa T \times \ln 2 \tag{2.3}$$

On the other hand, the theoretical limit of energy consumed during communication $E_{com,u}$ is given by the free-space path loss ($FSPL$) of the physical channel since the transmitter (Tx) still needs to transmit a power level which needs to be more than the receiver's (Rx) sensitivity after considering the channel loss. This is under the assumption that the receiver consumes zero power and the transmitter has a 100% efficiency. ($FSPL$) calculated using Frii's equation [23] [24] and is shown in Eq. (2.4), where A_{Tx} and A_{Rx} are the antenna gains of the transmitter and receiver; λ is the wavelength, d is the distance between the transmitter and receiver, and n is an empirical parameter that represents fading margin (typically between 2 to 3).

$$FSPL = A_{Tx}.A_{Rx}(\frac{\lambda}{4\pi d})^n \tag{2.4}$$

For a typical sub-GHz protocol operating in the ISM band at 916 MHz with $d = 10$m, $FSPL$ can be estimated to be 48 dB ($n = 2, A_{Tx} = 2$ dB, $A_{Rx} = 2$ dB). If a state-of-the-art Rx which has a sensitivity of -120 dBm is used in the system,then the Tx needs to transmit a minimum of -72 dBm. This translates to a power consumption of 63.096 pW as theoretical minimum for power consumption. The typical data rate (DR) for sub-GHz communication is 5kbps. This results in a theoretical minimum energy efficiency of $(E_{com,u})_{th\_min} = 1.262 \times 10^{-14}$ J/bit, which is more than 10^7 times higher than computational minimum given by Landauer's principle.

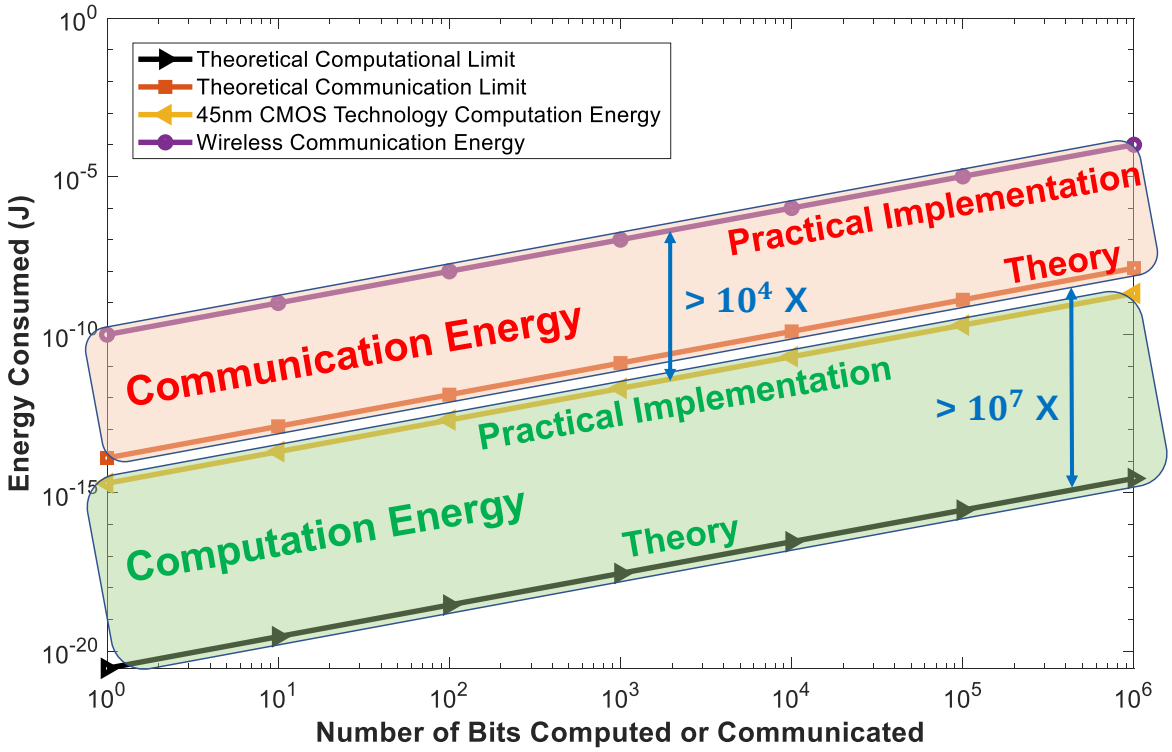

Figure 2.7. Comparison between theoretical and practical computation and communication energies [25] [26] shows that computation energy is 10^4 times less than communication energy for the same number of bits with leakage current ignored [5].

HDL simulations of in-sensor analytics in standard 45nm CMOS process resulted in 80 μW power consumption at 100 MHz and a linear increase in computation energy at a rate of $\approx$2 fJ/bit [5]. The preceding discussion is summarized in Fig. 2.7 wherein the contrast

between E_{com} and E_{cmp} is shown for the same number of bits transmitted, or switched [25]. Despite advances in wireless communication transceivers[26], computation saves at least 10^4 times more energy than communication for the same number of bits processed. This makes a strong case for incorporating in-sensor analytics to process and selectively transmit data for reducing the overall system power consumption, especially when harvested energy is a scarce commodity. This conclusion is valid while the ratio between the number of bits switched during ISA and the reduction in the number of bits transmitted is less than (E_{com}/E_{cmp}), which we anticipate during normal operation.

Communication Energy and Accuracy Trade-off

For a long-range sensor node that samples and transmits data every N seconds, over n seconds the communication module is on for a total time of $T_{comm} = \frac{bits \times n}{baud \times N}$. The total energy consumed during n seconds is then represented by Eq. (2.5).

$$E = (T_{com}.I_{com} + T_o.I_{cmp,lkg} + 2.T_{tran}.I_{com}.\frac{n}{N}) \times V \tag{2.5}$$

Where I_{com} is the current consumption of the communication module (along with computation of the network stack and leakage), $T_o = (n - T_{com})$, $I_{cmp,lkg}$ is the computation and leakage current consumed during sampling and data processing when the communication module is off, and T_{tran} is the transient time during switching the module on and off (hence the factor 2) added to the initialization time. Eq. (2.5) makes it evident that when $T_{com} \ll 2.T_{tran}.\frac{n}{N}$ (i.e. when $\frac{bits}{baud} \ll 2.T_{tran}$), communication energy is limited by the energy required to turn the module on or off. Conversely, when $2.T_{tran} \ll \frac{bits}{baud}$, communication energy is limited by the payload size or the number of bits transmitted. In practice, $2.T_{tran}$ is usually a few ms long [16] and the data rate is much larger than the number of bits per sample, resulting in communication energy being primarily limited by the energy required to turn the module on or off and its frequency.

In an effort to reduce power consumption previous methods in literature (for example, [7], [27]) preferred a duty cycle based approach to limit the amount of switching energy by increasing N.This results in an increased probability of losing important, useful information.

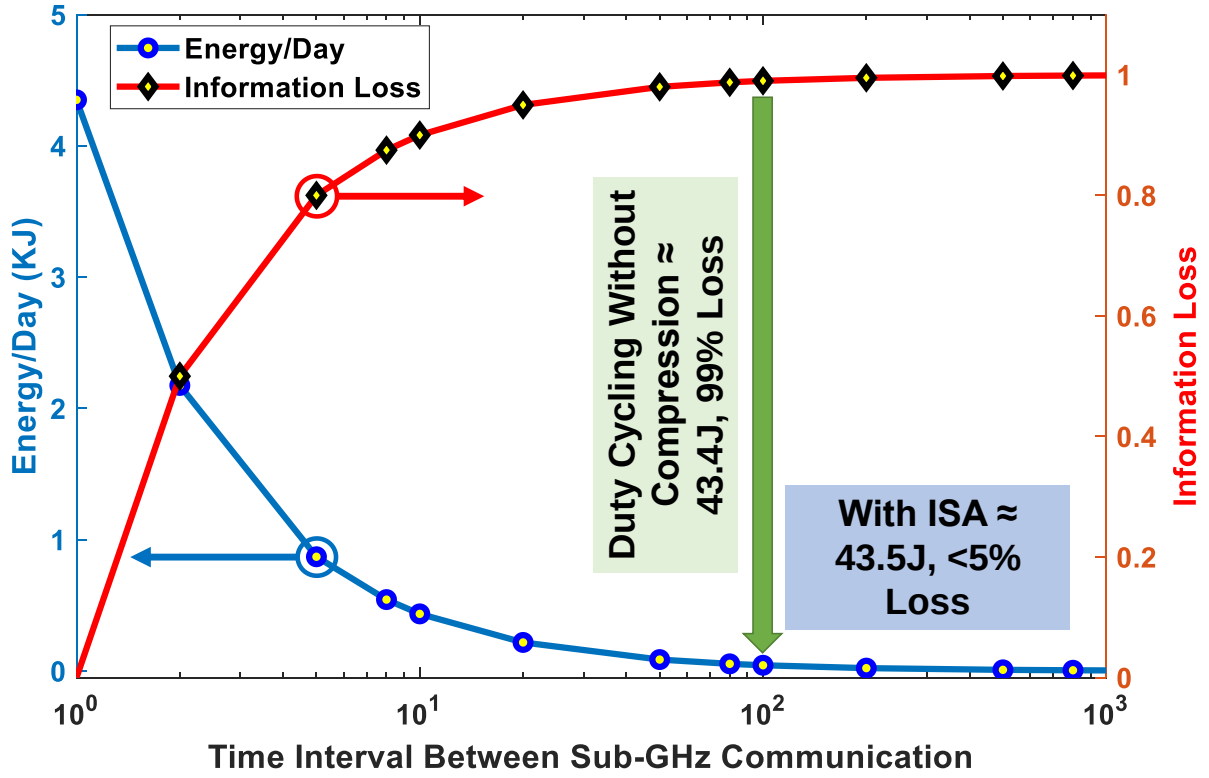

Figure 2.8. Information loss and communication energy as a function of the time interval between sub-GHz transmission of samples, motivating the need for in-sensor analytics.

Fig. 2.8 illustrates this scenario by graphically depicting the communication energy per day and rate of information lost as a function of N. The values were measured for LoRa communication in a Nordic nRF52 platform [5]. Comparing $N = 100$ to a baseline of $N = 1$, we see a 50X reduction in energy consumed at the cost of 99% loss of information. Implementing a mechanism to avoid these losses while taking an acceptable hit in energy consumption makes a strong case for utilizing finely tuned in-sensor analytics and energy aware adaptive transmission.

Interaction Between Energy Harvested, Storage Capacity, and Information Transfer Rate

So far the discussion has covered the minimum energy generated by the energy harvester and software solutions that can be implemented to reduce energy consumption in order to meet that design constraint while minimally affecting performance. However, limiting the device operation to the minimal power budget will waste massive amounts of energy harvested throughout the year and potentially lose information that could have otherwise been reported. These losses can be subverted by making the device energy-aware, such that it can vary its energy consumption by altering the information transfer rate based on the amount of energy available.

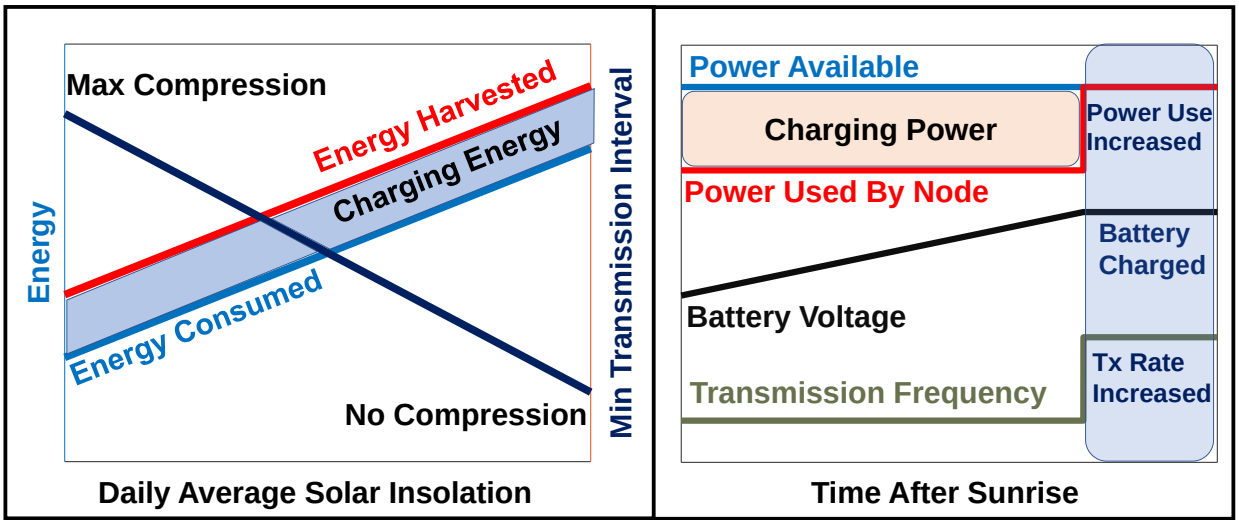

Figure 2.9. Device behaviour shown as the relationship between the harvested energy, energy consumed by the node, charging energy or battery voltage, and long range communication transmission interval shown as a function of daily average solar insolation and time after sunrise on a particular day.

The average energy consumed by the device (E_{avg}) for a specific time interval between communication samples can be simplified to Eq. 2.6. I_{comm}, I_{comp}, and I_{off} is the current consumed during communication, computation, and standby mode respectively; and T_{comm}, T_{comp}, and T_{off} is the time spent performing each of those tasks. As the information transfer

rate or frequency of reporting samples increases, the relative value of T_{comm} to the total time increases which thereby increases energy consumption.

$$E_{avg} = V(T_{comm}.I_{comm} + T_{comp}.I_{comp} + T_{off}.I_{off}) \tag{2.6}$$

As shown in Fig. 2.9 the energy harvested by the node increases with the increase in average solar insolation received during a day. Therefore, the device can safely transmit data at a higher transmission rates throughout the entire day while keeping the total energy consumption within the bounds of the total amount of energy available. The higher transmission rates will reduce the loss of information without comprising the ability of the device to perpetually function since the energy used to charge the battery will remain constant. This will translate to higher transmission rates in the summer months when more energy is available from the harvester and consequently lower transmission rates in the winter.

During daylight hours the difference between the harvested power and the power consumed by the node is used to charge the energy storage device as shown in Fig. 2.9. When the harvested power increases beyond the minimum power consumption of the device the battery starts charging. As the sunlight intensity changes throughout the day, the data transmission rate is varied such that the amount of charging power remains constant. If the energy storage device is charged to capacity, the excess power available from the energy harvester would be wasted if not consumed by the device. Therefore the power consumed by the wireless sensor node is increased to match the amount of power generated by increasing the data transmission rate.

2.2.3 Platform and Implementation

Hardware

The custom long range sensor node shown in Fig. 2.10 can be broadly divided into three main blocks, power management, the microcontroller and RF chain, and the environmental sensors. The device was designed to be modular and consists of two vertically stacked printed circuit boards (PCB). One PCB (top) houses only the environmental sensors to allow for easy replacement or addition of new sensors to re-purpose the device without redesigning

the entire sensor node. The top layer of the bottom PCB comprises of the microcontroller and RF chain along with the power sensor and finally, the energy harvester and battery management is placed on the bottom layer.

Figure 2.10. PCB stack of the CC1352 based energy harvested long range sensor node shown along with its 3D printed housing. 50mm x 60mm amorphous silicon solar cell, with BQ25505 (TI) energy harvester used for power management. CC1352 SoC (TI) is used to implement ISA+EICO in conjunction with the power sensor (INA233). HDC2010 and OPT3001 is used as the environmental senors.

A System-on-Chip (CC1352R1, Texas Instruments (TI)) integrates an ARM Cortex-M4F processor with a multi-band (sub-GHz and Bluetooth low energy) wireless transceiver. In this design only the sub-GHz wireless transceiver is used and the BLE transceiver is always in the powered down state. The primary motivation for selecting this SoC was minimizing power consumption while maximizing performance since it boasts of one of the lowest power architectures with high receiver sensitivity (-121 dBm for 868MHz at 5.8mA) and transmission power efficiency (+14dBm for 868MHz at 28.9mA). An integrated ultra-low power sensor controller is used to sample and process sensor data whose operation is independent of the system processor and draws 30uA at 2MHz. The system CPU consumes 2.9mA in active mode at 48MHz and 0.85uA in stand-by mode with 80KB of RAM and CPU retention, making it powerful enough to run analytics by consuming minimal power. Finally, power consumption is further reduced by using an on-chip DC-DC converter.

Three environmental variables temperature, humidity, and light intensity are collected by the sensor node over I2C. HDC2010 and OPT3001 by TI are used to measure the first two and the last quantity, respectively. HDC2010 provides data at an accuracy of 0.2 degrees Celsius for temperature and 2% for humidity while consuming 0.55uA. OPT3001 has a measurement range of 0.01 lux to 83K lux in the visible spectrum. The sensors are powered up through a PMOS in order to turn them off during sampling intervals and conserve power.

An amorphous silicon solar cell of 60mm by 50mm is used as the power source to an ultra-low power harvester and power management IC (BQ25505, Texas Instruments). The device has cold start voltage of 600mV, consumes 325nA, performs maximum power point tracking, and can continuously harvest energy when the input voltage is as low as 100mV. The energy harvester converts the solar cell voltage to 4.2V, which is used to power the system and charge the back up battery/charge storage device. When the input power falls below the system load, an inbuilt automatic power multiplexer draws power from the charge storage device to prevent the voltage rails from drooping. The sensor node is made energy aware by measuring the battery voltage and the power drawn from the solar cell on the high side using an ultra-precise power monitor (INA233 by TI) which typically draws 310 μA during normal operation and 2 μA in standby mode.

Software

The microcontroller is programmed with an RTOS to read the sensor values every 1 second and run a network stack (Easylink by Texas Instruments) for sub-GHz communication. Data is transmitted at an interval between 1 second (no compression) to 5 minutes (maximum compression). A lightweight algorithm is implemented for anomaly detection and energy-aware data transmission to optimize power consumption and loss of information.

```
Data: Output power of solar cell
Result: Data Transmission Rate
initialization;
while power reading available do
    Integrate for Energy Available;
    if harvested power > 0 then
        if power reading above threshold then
            Increase data transmission rate;
        else if power reading below threshold then
            decrease data transmission rate up to minimum Tx rate;
        else
            if Battery charged then
                Set data transmission rate to match available power;
            end if
        end if
    else
        if Sunset Time then
            Measure battery voltage and compute energy stored;
            Calculate new minimum transmission rate;
        end if
    end if
end
```

Algorithm 2: Energy-aware data transmission algorithm

The sensor node is made energy intelligent by measuring the amount of energy harvested on a given day and the energy stored in the battery to determine the minimum energy consumption of the device for the following day. This is achieved by controlling the communication energy through adjusting the minimum transmission rate of the device, which governs the information transfer rate at nighttime and until the harvested power exceeds the power consumption of the sensor node during the day. The minimum transmission rate is evaluated from the energy measurements once every day at sunset, when $P_{Harvest}$ falls to

zero for the first time. The energy harvested on a given day is shown in Eq. 2.7. The power sensor connected to the solar cell is sampled once every minute and numerical integration is performed to calculate the energy in Joules. Eq. 2.8 depicts the calculation of the energy stored in the battery which is performed by using a look up table on the measured battery voltage. The look-up table was generated by characterizing the battery at a dais charge rate of 0.1C (23mA).

$$E_{Avail}(J) = \Sigma(P_{harvest} * 60/1000) \tag{2.7}$$

$$E_{BATT}(J) = f_{BatteryChemistry}(V_{BATT}) \tag{2.8}$$

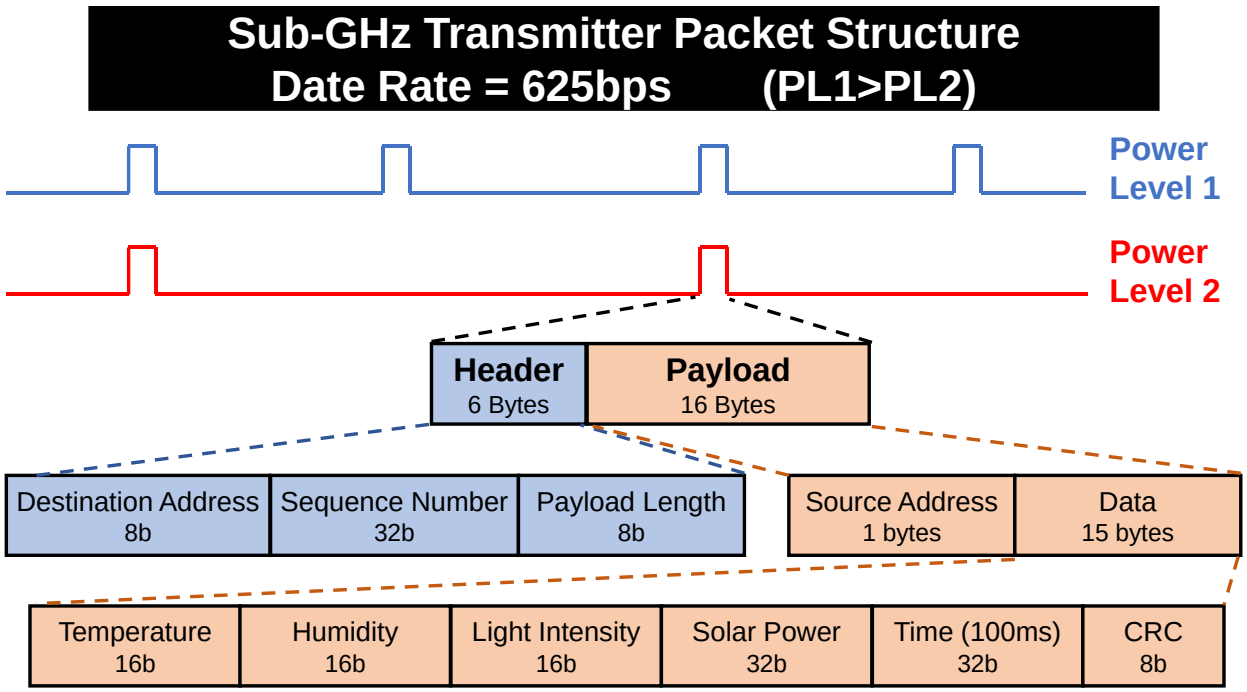

Figure 2.11. TI Sub-GHz (Easylink) packet structure at 625 bps for long range communication. Every Tx packet 22 Bytes long with a header of 6 Bytes and payload of 16 Bytes. Packet transmission rate varies based on the total energy available to the wireless sensor node.

The available energy range is divided into 10 regions which maps on to a data transmission rate between 1 sample/second (no compression) to 1 sample every 300s (maximum

compression). As shown in Fig. 2.11, each data packet is 22 bytes long carrying 16 bytes of payload. Sensor data of humidity, temperature, and light intensity is contained within 6 bytes, and 4 bytes are used to convey the time of sampling. 4 Bytes are also used to transmit information on the available power. Each device also sends its specific software defined address and error detecting codes.

```
Data: Samples from environmental sensors
Result: Anomalies detected in sampled data
Initialize the threshold (x) of the k-means clustering algorithm;
while New sample available do
    if data >= x% or <= x% from last anomaly (ISA) then
        activate sub-GHz communication;
        send temporally compressed data stream to the receiver;
        record new transmission time; deactivate sub-GHz communication;
    else
        wait for the next anomaly/next transmission time;
        stay in low-power sense and compute mode;
    end
    if time since last transmission = transmission interval then
        activate sub-GHz communication;
        send current data point to the receiver;
        record new transmission time; deactivate sub-GHz communication;
    else
        wait for the next anomaly/next transmission time;
        stay in low-power sense and compute mode;
    end
end
```

Algorithm 3: Anomaly Detection followed by data transmission using Long Range communication at a particular power level

The anomaly detection algorithm is used to minimize the loss of information when lower data transmission rates are used. It incorporates a predefined threshold for each environmental variable being sensed. When the difference between the sensed data and the previous anomaly value crosses this threshold an anomaly is registered and data from all sensors is transmitted. These thresholds were calculated offline using a k-means clustering algorithm over a span of more than 4 weeks.

Figure 2.12 shows an example of humidity data transmitted by the sensor node using anomaly detection overlaid on all of the samples collected by the microcontroller. In this case

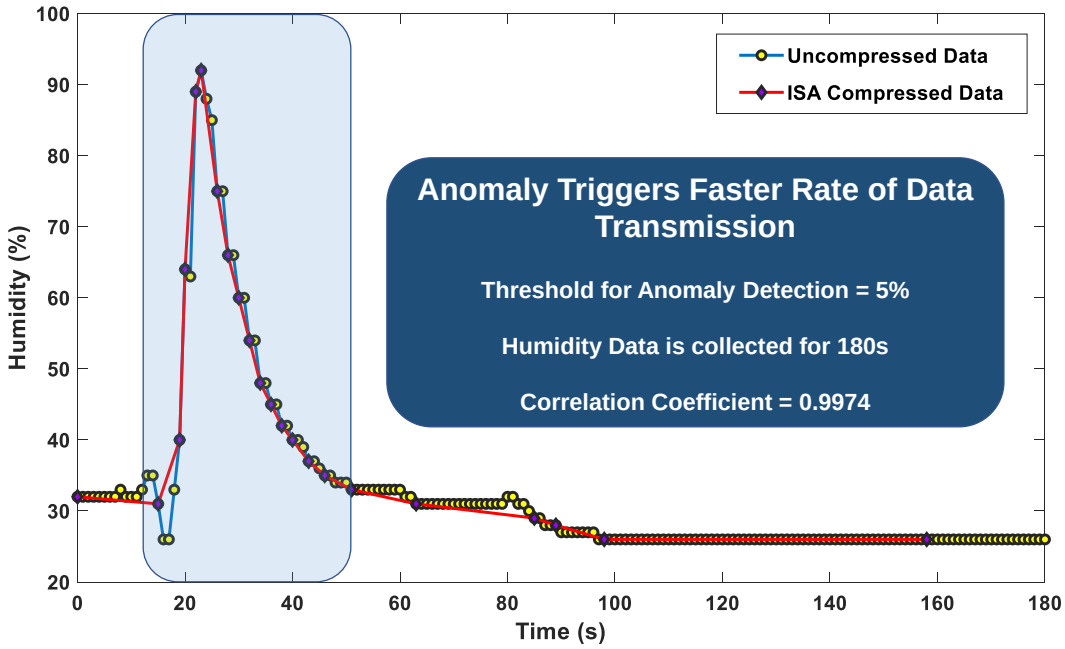

Figure 2.12. An example of humidity data logged from HDC2010 with and without anomaly detection at a threshold of 5%.

a sampling frequency of 1Hz was used and 180 data points were collected. The threshold for anomaly detection was set at 5% with a data transmission interval of 60s. As seen a total of 23 data points were transmitted resulting in a temporal compression ratio of 7.83. Of these 23 data points, 21 were transmitted due to the anomaly created between 15s and 100s and 2 were transmitted during normal operation. Without the introduction of an anomaly the compression ratio would have been much higher. The compressed data has a correlation coefficient of 0.9974 with the original sampled data.

A report of every 1 degree Celsius change in temperature is desirable since the sensor node is primarily used for agricultural and environmental monitoring purposes. Temperatures in Indiana remain between -20 to 20 degrees Celsius for most of the year and a 5% threshold will prevent loss of information irrespective of the data transmission interval. In the summer months when the temperatures cross 20 degrees Celsius, the anomaly detector will not trigger at every degree change in temperature. However, the sunlight intensity also increases in this

time period which will result in faster minimum data transmission rates to prevent any loss of information.

2.2.4 Results

Energy Consumed by the Wireless Sensor node

The current consumption of the sensor node in different modes of operation is measured using a precision current-voltage analyzer (B2901A, Keysight) and shown in Fig. 2.13. In standby mode the device consumes $280\mu A$, during computation $3.5mA$, and a peak current of $35mA$ for sub-GHz long range transmission at an output power of +14dBm. At a supply voltage of $3.7V$, this translates to a power consumption of $1.036mW$, $7.03mW$, $12.95mW$, and $129.5mW$ during standby, sampling, computation, and communication respectively. During each sampling interval, which repeats every 1 second, the microcontroller SoC spends approximately $999ms$ in standby mode, $200\mu s$ to sample the sensors, and $800\mu s$ to implement the various algorithms, resulting in an energy consumption of $1.04mJ$. Each computation interval can vary between 1s to 300s, during which the SoC spends $282ms$ transmitting the sub-GHZ RF packet at the cost of standby time, resulting in a communication energy of $33.25mJ$. The standby (leakage) current is relatively high since an ultra-low noise, high PSSR, RF, low-dropout linear regulator was selected for the design which had a typical ground pin current of $265\mu A$. The current consumption and consequently the energy consumption can be driven down by selecting an alternate voltage regulator, however, we did not make this choice since the energy goal of our design was met.

The energy profile for the CC1352-based energy harvested sensor node is presented in Fig. 2.14 for each of its different data transmission intervals. The fastest data transmission rate of every 1 second (no compression) occurs either during the highest range of sunlight intensity, or when the net available energy permits a daily energy consumption of $2872.5J$. The slowest data transmission rate of once every 300 seconds (maximum compression) occurs either when negligible amounts of energy was harvested during the previous day (due to snow accumulation, etc.) or the net available energy is at a critical value to prioritize charging of the battery. This mode consumes an average energy of $90.1J$, which translates to a

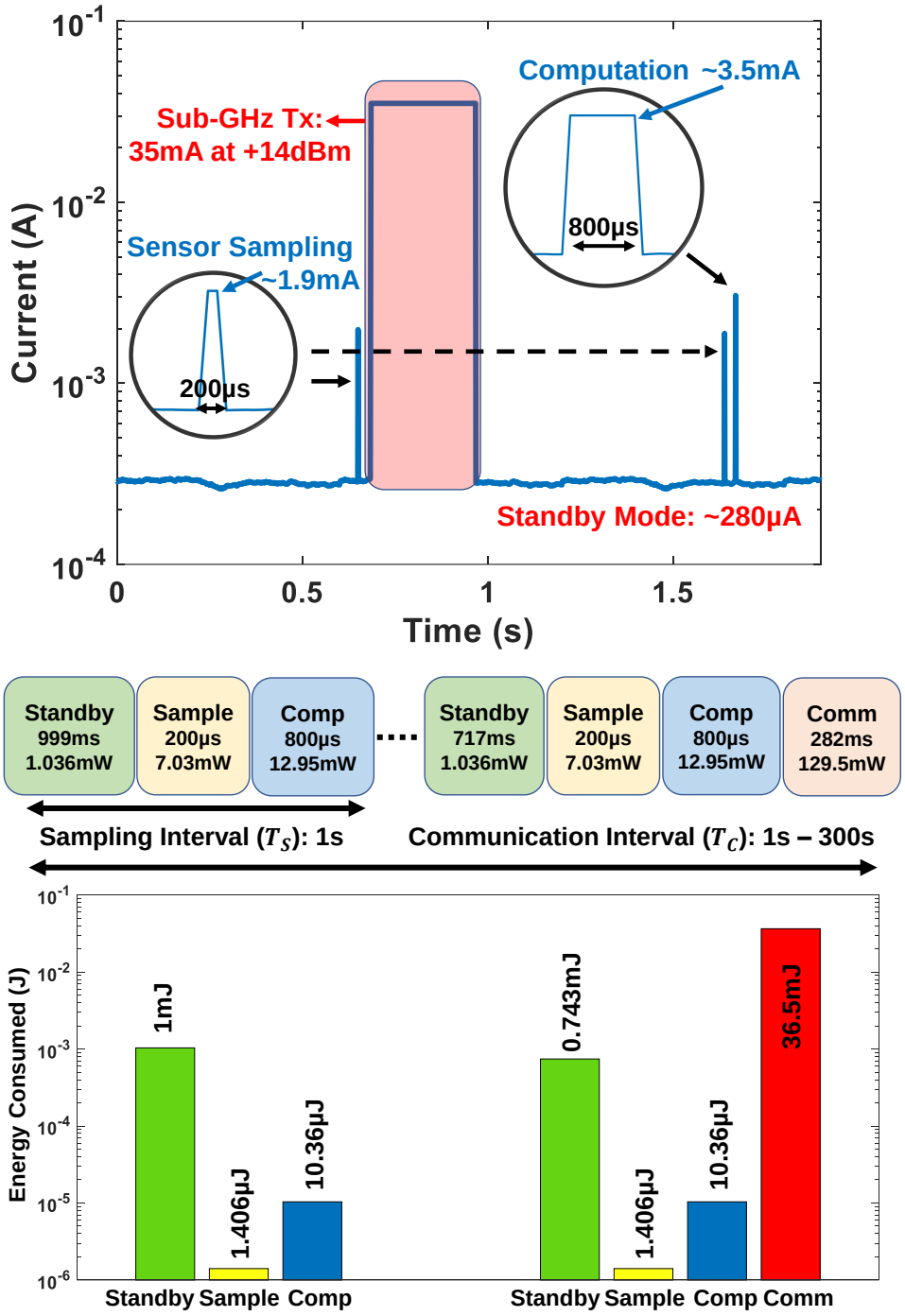

Figure 2.13. Current consumed by the wireless sensor node as measured by a precision current-voltage analyzer and the amount of time spent and power and energy consumed in each of its different modes of operation i.e. standby (leakage), sampling and computation, and communication.

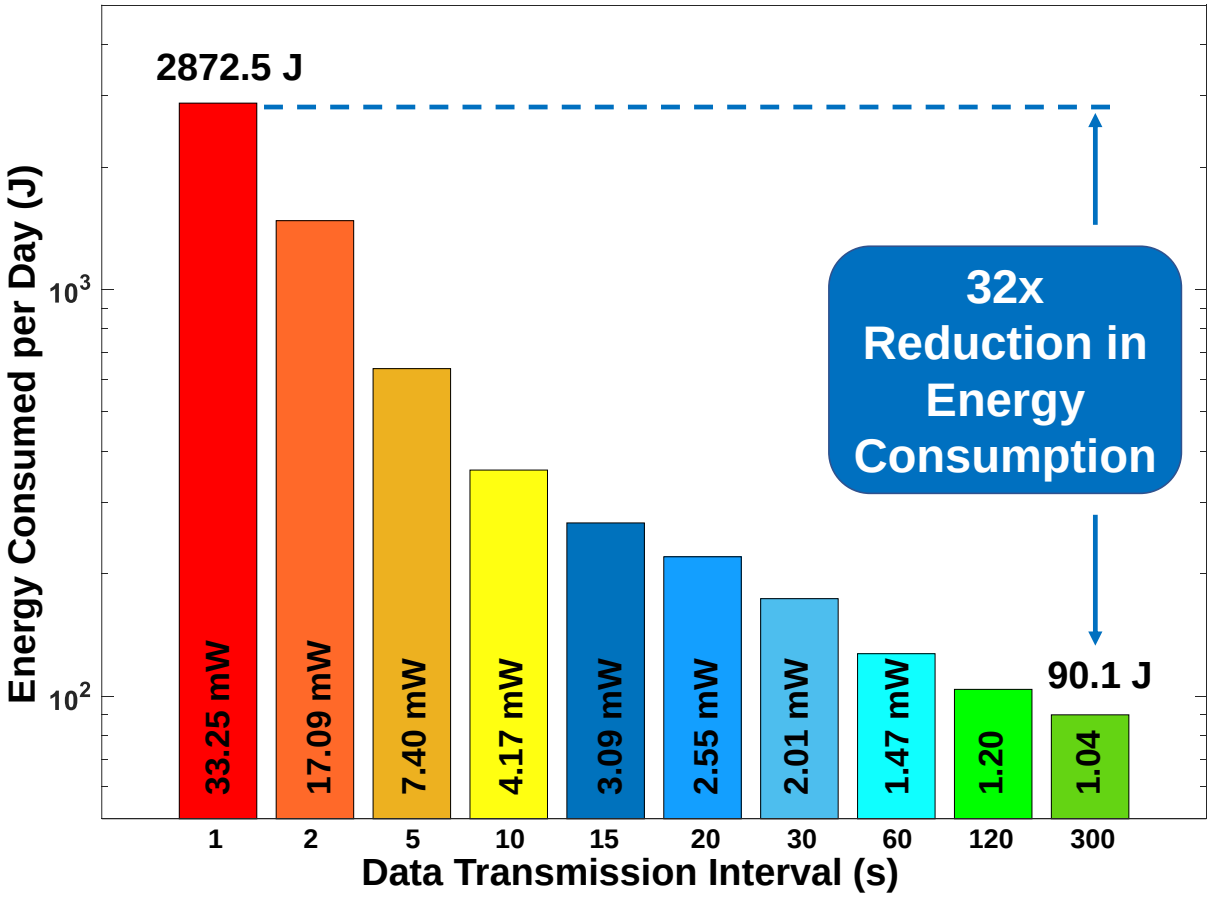

Figure 2.14. Average energy consumed by the wireless sensor node in one day in each of its different data transmission modes used to report sensor data.

32x reduction in energy consumption with less than 5% loss of information. In case the energy harvester is incapacitated due to excessive accumulation of snow or other unforeseen circumstances, a lifetime of between 336 hours (14 days) to 818 hours can be obtained based on the amount of energy stored in a standard $230mAh$ battery.

Interaction Between Energy Available, Energy Consumed and Transmission Rate

The energy harvester and power management system were characterized by measuring the power available at the microcontroller supply net using a solar simulator which generated a sunlight intensity of $1KW/m^2$, also called as 1 sun or peak sun. The results obtained from this setup were multiplied by the peak sun hours seen in a day seen in Indiana during a given

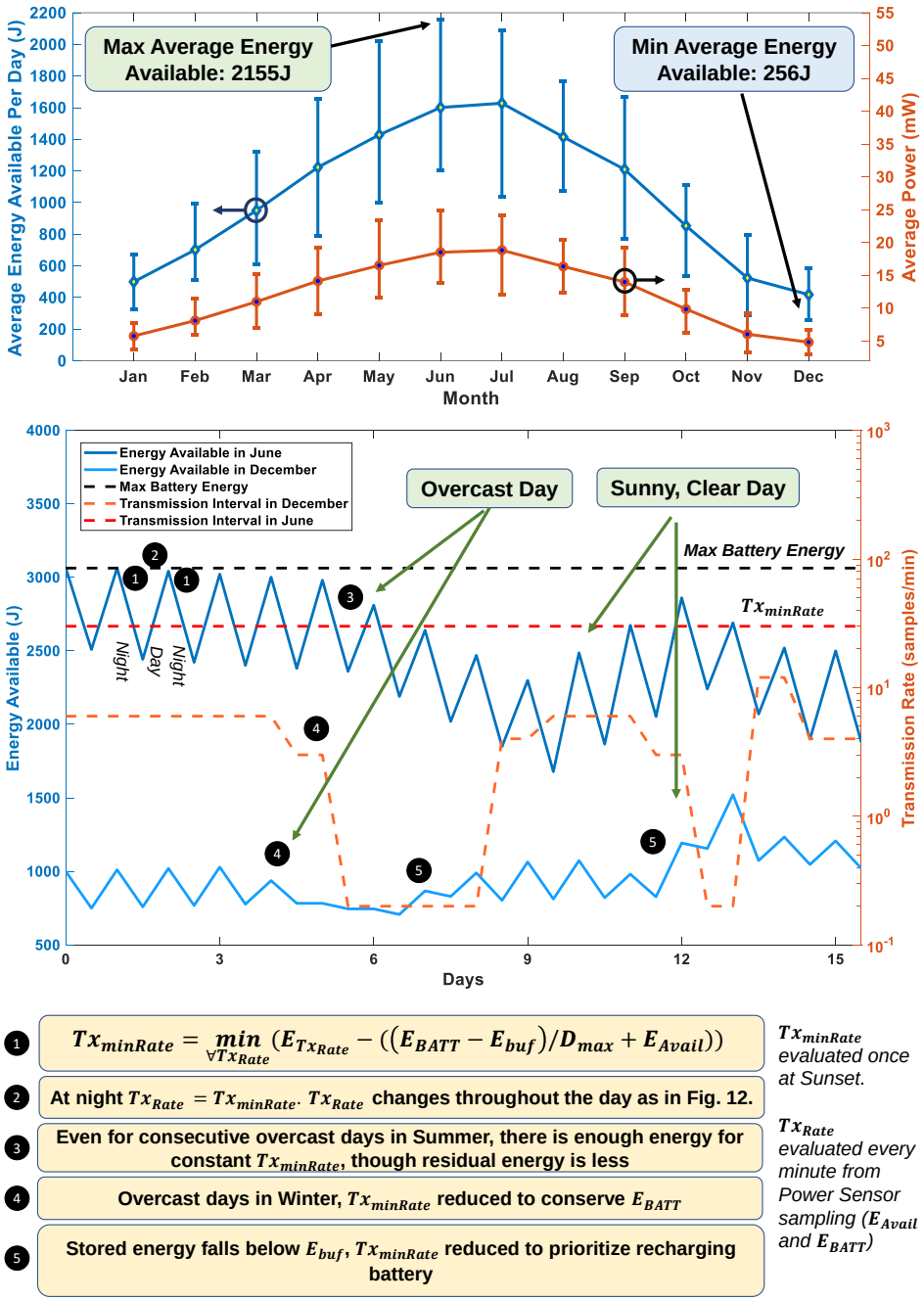

Figure 2.15. (a) The maximum, minimum, and average power and energy available from the 50x60mm amorphous silicon solar cell in a 24-hour period on an average day of the given month in Indiana. This accounts for the losses in the energy harvester and power management system. (b) The minimum data transmission rate of the wireless sensor node as a function of energy available during a 15 day period at different times of the year.

month to calculate the maximum, minimum, and average energy harvested on a given day of each month of the year. This is shown in Fig. 2.15 along with the equivalent available power for a 24 hour period, such that the charge storage device sees a net zero power loss. These power measurements reflect a horizontal placement of the solar cell which will be typical during the course of using the device. Obviously, the instantaneous power available during peak sunshine hours can be up to 3X higher than the average value. The average minimum energy value of 256J in December is almost 3 times the minimum energy consumed by the device and perfectly accommodates daily fluctuations in weather and the reduction in efficiency over time due to the accumulation of dust.

$$Tx_{minRate} = \min_{\forall Tx_{Rate}} (E_{TxRate} - (\frac{E_{BATT} - E_{buf}}{D_{max}} + E_{Avail})) \tag{2.9}$$

Eq. 2.9 describes the relationship between the amount of energy harvested on the previous day (E_{Avail}), energy stored in the battery (E_{BATT}), and minimum data transmission rate ($Tx_{minRate}$) which governs the energy consumed by the node. The equation assumes that at least E_{Avail} will be harvested in the subsequent days and based on the amount of energy stored, it determines whether to give charging preference or allow the sensor node to burn extra energy such that it wont reach its critical threshold (E_{Buff}) for D_{max} days. This net energy is compared to the energy consumption of each data transmission rate to find the closest match and determine the minimum data transmission rate for the following day. E_{buf} represents the buffer energy in the battery (critical threshold) which must be maintained to accommodate for future bad predictions when energy availability is low.

Fig. 2.15 depicts the operation of the device over 15 days during both, the summer (June) and winter (December) months. The upward slopes depict charging of the battery during day time and the downward slopes for discharge during night time. During the summer months the minimum transmission rate remains steady at 30 samples/minute despite any changes in weather conditions which varies the amount of energy harvested and subsequently stored in the battery since the net energy available never moves between thresholds. An interesting point to note is that the device never enters the highest minimum transmission rate even on sunny, clear days, when maximum energy is harvested. This can be rectified by either using a

larger battery, solar cell, or placing the device in a geographical location where more sunlight is available. During the winter months, the energy stored in the battery is typically lower and large fluctuations are seen in the minimum transmission rate due to changes in weather conditions to conserve the energy stored in the battery, such that the device can remain operational. When the energy stored in the battery reaches the critical threshold of E_{buf}, we can see the device prioritizes charging by drastically reducing the minimum transmission rate to reduce power consumption even when large amounts of energy was harvested.

During any given day, the relationship between the power available from the energy harvester, power consumed by the wireless sensor node, the energy stored, and data transmission interval is shown in Fig. 2.16. This example depicts a sunny, clear day in March, in Indiana. At night time the device transmits data at the daily minimum data transmission rate which is a function of the total energy available and is depicted in Eq. 2.9. In this example 12 samples are transmitted every minute at a power consumption of 7.40mW. Over the course of that night which was 717minutes long, 318.35J of energy was consumed. At day break, the power available from the energy harvester slowly starts to rise and eventually becomes greater than the power consumed by the device and the excess power starts to charge the battery. When the available power is 2.5X the power consumed by the device (60% of available power for charging), the sensor node switches to a higher data transmission rate. This continues as long as the available power increases or the battery is completely charged. Once fully charged, the device transmits data at the highest possible rate, such that its power consumption is within the bounds of available power.As the available power reduces with decreasing solar insolation, the data transmission rate decreases until it reaches the newly calculated minimum transmission rate for the following day.

Accuracy of Data Reported at Maximum Compression

Fig. 2.3 shows data from two sensor nodes, device 1 functioning at maximum compression and device 0 functioning at minimum compression (no compression) placed at the same location. For demonstration purposes, the devices were placed in these modes by emulating the power sensor readings to replicate the maximum and minimum power obtained from the

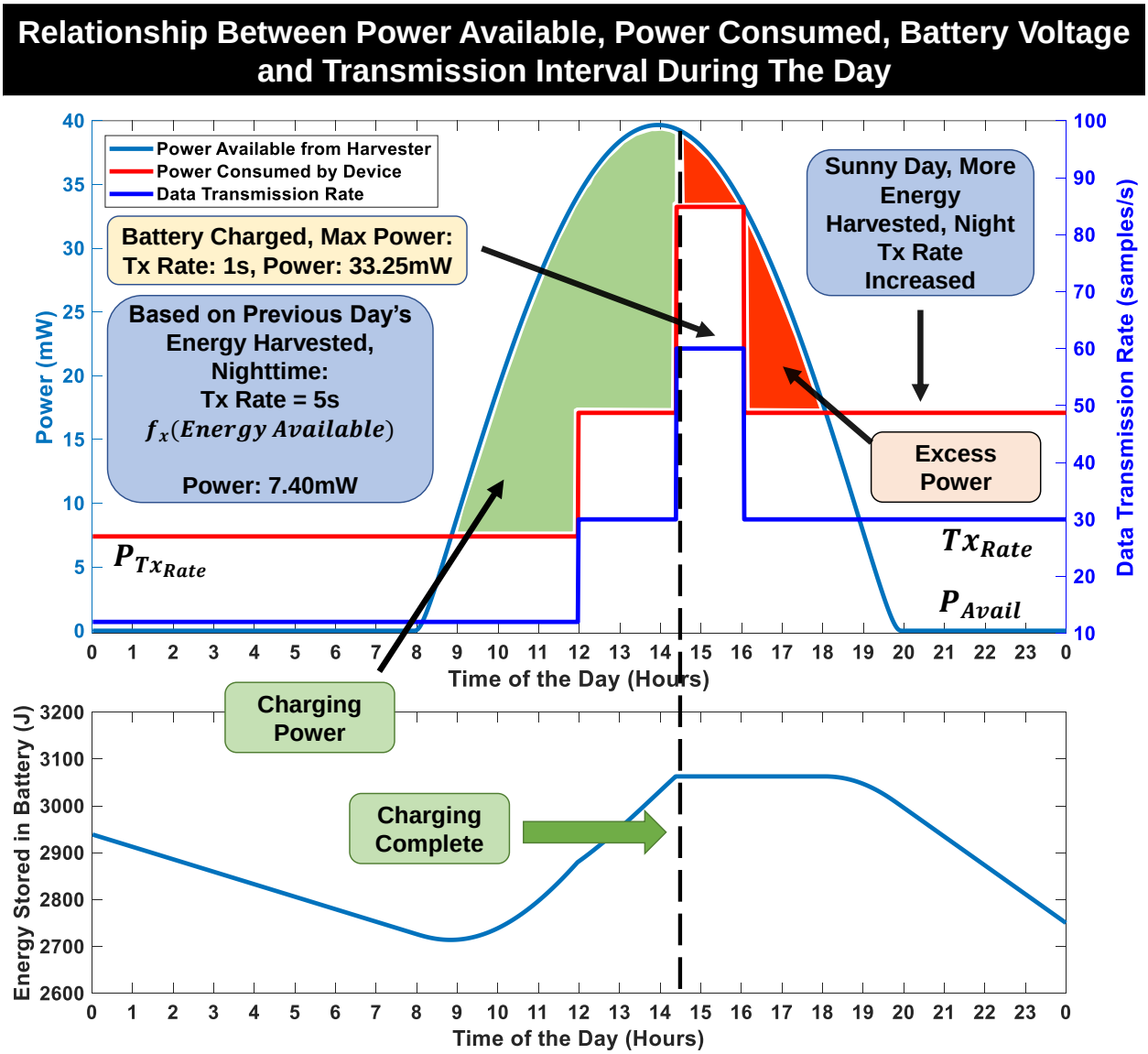

Figure 2.16. Interaction between power available, power consumed, energy stored in the battery, and data transmission rate during the course of a sunny, clear day during March in Indiana.

solar cell. Additionally, to demonstrate the difference in readings reported by the devices, temperature and humidity anomalies were artificially created using a heating pad and a cooling fan which was programmed to turn on for 1 and 5 minutes respectively, once every hour. Device 1 transmits data once every 5 minutes and reports temporally compressed data when the anomaly occurs. Whereas, device 0 transmits uncompressed data every second to make maximum use of the available power. Sensor data of temperature and humidity

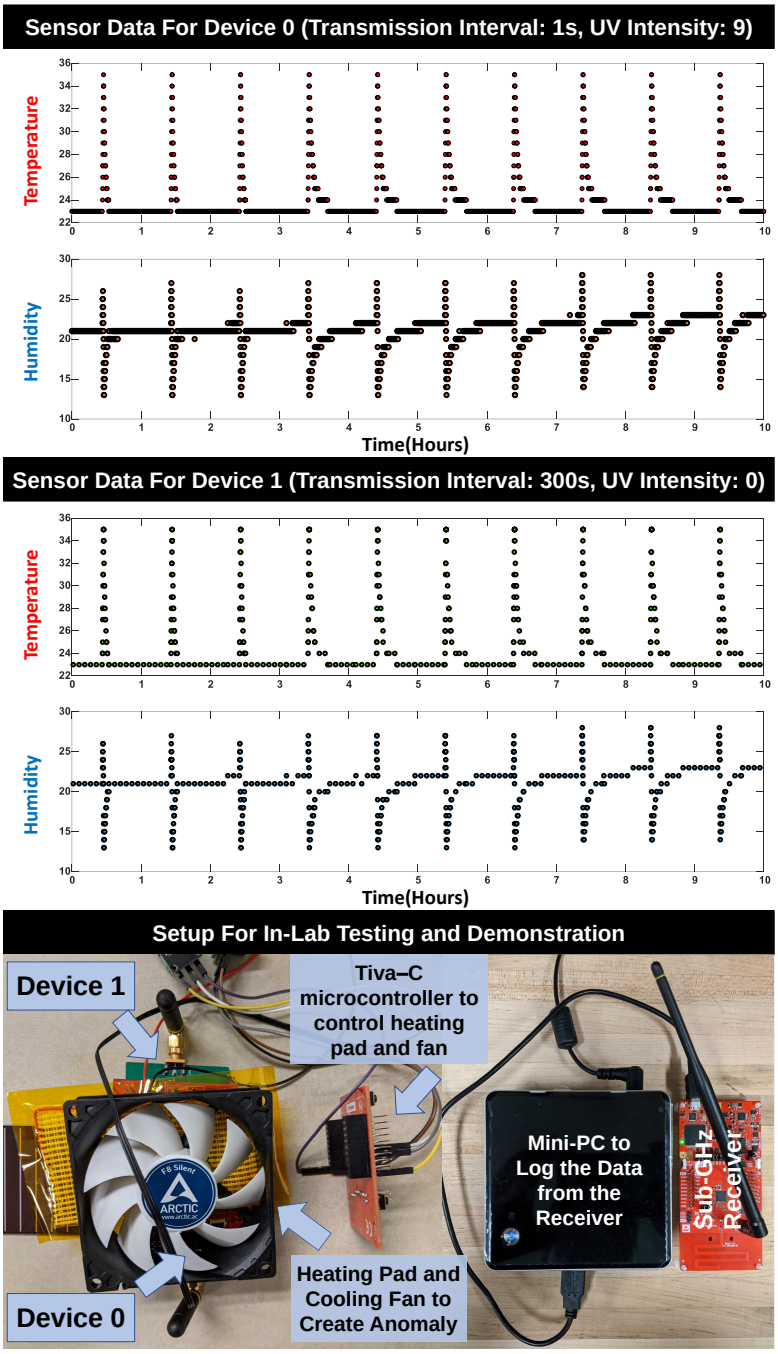

Figure 2.17. Device 0 and Device 1 are placed at the same location with a heating pad and cooling fan placed on top of them to artificially create anomalies in their sensor readings for demonstration purposes. Device 0 operates in the maximum net energy available mode by transmitting data every second, whereas device 1 operates in the minimum net energy available mode by transmitting data every 300 seconds.

obtained from the receiver was logged in a comma separated value (.CSV) file on a mini-PC. That data was processed and displayed in MATLAB as a time-varying quantity. A total of 418 data points were transmitted by device 1 as compared to 36000 by device 0, which resulted in a net compression ratio of 86.125 and a correlation coefficient of 0.9937 and 0.9808 for temperature and humidity respectively. This demonstration displayed a maximum energy savings of approximately 32X, due to the difference in the transmission rate of the two devices.

2.2.5 Conclusion

In this paper we analyzed the trade-offs and proposed the hardware design and software methods to implement a perpetually powered, energy-harvested and aware, long-range communication sensor node which can function with a minimally sized harvesting element. This was achieved through Energy-Information Dynamic Co-optimization, which was termed as EICO. The proposed method varied the data transmission rate of the wireless sensor node to optimize its energy consumption based on the total amount of energy harvested and stored in the battery. This resulted in nearly continuous transmission of samples in the summer months because of large amounts of energy harvested, to a steady decrease to low data transmission rates during the winter months due to a lack of energy availability. To minimize the loss of information due to steep duty cycling of data transmission rates, in-sensor analytics was employed to detect anomalies and enable event driven communication and temporal data compression. This resulted in daily energy consumption levels spanning between 90.1J to 2872.5J, an approximately $32X$ difference based on the time of the year, energy collected by the harvester, and energy stored in the battery. Despite these transmission rate fluctuations and steep duty cycling, the correlation coefficient between the transmitted sensor data and sampled sensor data was always > 0.95, resulting in $< 5\%$ loss of information.

Although this design primarily focuses on solar power as the energy source, it can be easily modified to work with alternative sources like TEGs and piezoelectric generators to achieve an identical performance. As future work, the energy consumption would be analyzed throughout the year to ensure reliability over different weather conditions and network

security can be improved. Additionally, since the leakage current of the sensor node is the limiting variable for power consumption, a custom SoC can be designed in-house to significantly reduce leakage current and further miniaturize the sensor node. Subsequently, faster data transmission rates can be achieved with smaller harvesting elements.

3. DESIGN OF INTERNET OF BODY DEVICES

Most of the content in this chapter has been extracted verbatim from the papers:

S. Avlani, M. Nath, S. Maity and S. Sen, "A 100KHz-1GHz Termination-dependent Human Body Communication Channel Measurement using Miniaturized Wearable Devices," 2020 Design, Automation & Test in Europe Conference & Exhibition (DATE), Grenoble, France, 2020, pp. 650-653, doi: 10.23919/DATE48585.2020.9116556.

Sriram, S., Avlani, S., Ward, M.P. et al. Electro-Quasistatic Animal Body Communication for Untethered Rodent Biopotential Recording. Sci Rep 11, 3307 (2021).

https://doi.org/10.1038/s41598-021-81108-8.

M. K. Kim, C. Kantarcigil, B. Kim, R. K. Baruah, S. Maity, Y. Park, K. Kim, S. Lee,J. B. Malandraki, S. Avlani, A. Smith, S. Sen, M. A. Alam, G. Malandraki, and C. H.Lee, "Flexible submental sensor patch with remote monitoring controls for managementof oropharyngeal swallowing disorders,"Science Advances, vol. 5, no. 12, 2019.doi:10.1126/sciadv.aay3210.

3.1 EMG Device

3.1.1 Introduction

Successful rehabilitation of oropharyngeal swallowing disorders (i.e., dysphagia) requires frequent performance of head/neck exercises that primarily rely on expensive biofeedback devices, often only available in large medical centers, which directly affects treatment compliance and outcomes. The exponential scaling of transistors has enabled the production of wearable devices for fitness monitoring, medical diagnosis, and other applications. These devices are usually interconnected to relay sensor readings and other data, creating a local network known as Body Area Network (BAN). [28] These networks have been leveraged to create wearable and inexpensive remote monitoring system for the telerehabilitation of dysphagia. Here, we present the development and preliminarily validation of a skin-mountable sensor patch that can fit on the curvature of the submental (under the chin) area noninvasively and provide simultaneous remote monitoring of muscle activity and laryngeal movement during swallowing tasks and maneuvers. This sensor patch incorporates an optimal

design that allows for the accurate recording of submental muscle activity during swallowing and is characterized by ease of use, accessibility, reusability, and cost-effectiveness. Preliminary studies on a patient with Parkinson's disease and dysphagia, and on a healthy control participant demonstrate the feasibility and effectiveness of this system.

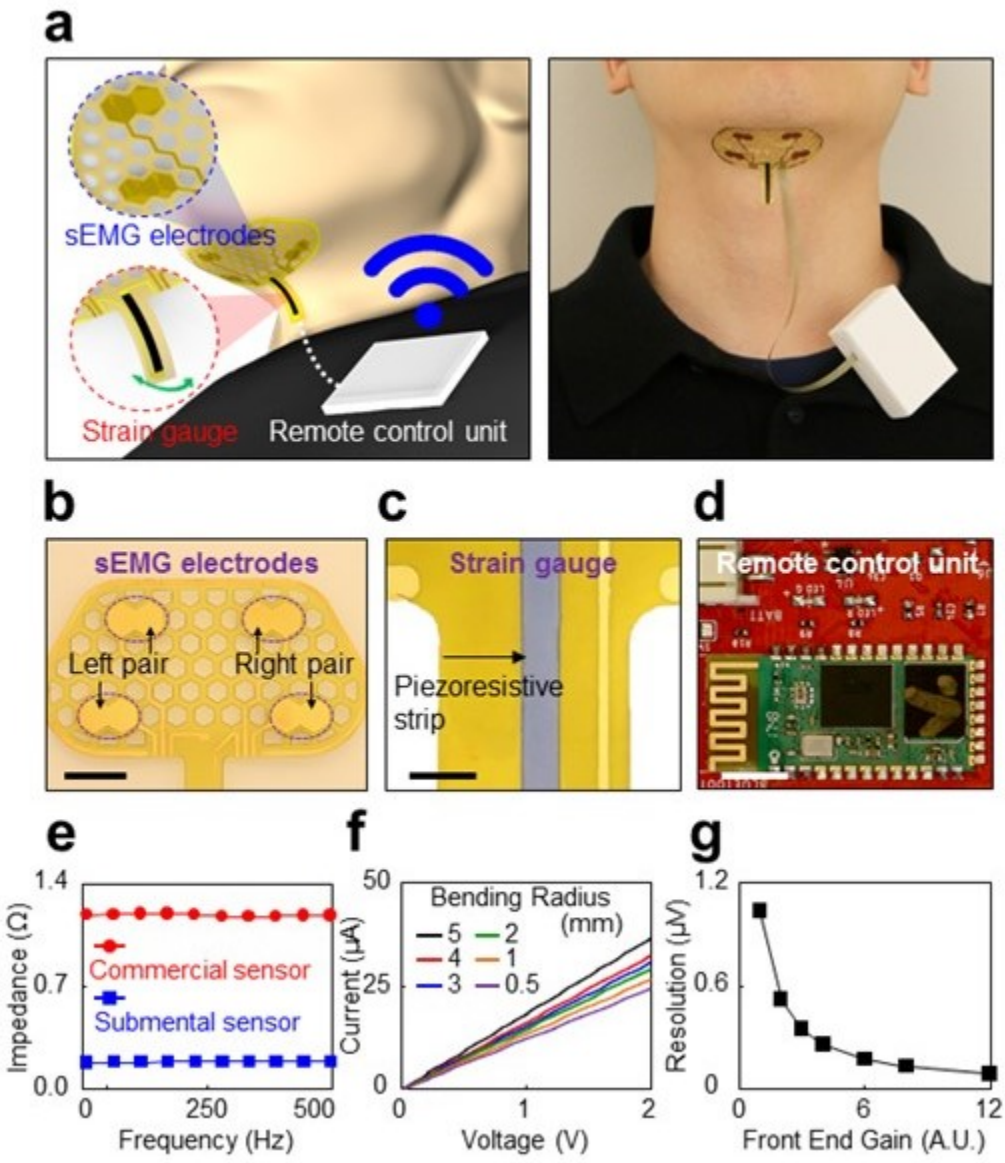

Figure 3.1. Custom-built wearable device for the telerehabilitation of dysphagia.

3.1.2 Portable Device for Remote Data Transmission

Fig. 3.1 shows an animated illustration and the actual photograph of the system. A sensor patch is mounted on to the submental area which incorporates embedded surface-electromyogram (sEMG) electrodes such that they remain in contact with the skin in a manner in which they are parallel to the underlying muscle fibres. The sEMG signals are measured by two pairs of electrodes through a double-differential recording. Additionally, the sensor patch integrates a piezoresistive strain gauge to respond against relative laryngeal movements during swallowing.

The portable unit for remote data transmission and powering is built on a 2-layer Printed Circuit Board (PCB) with commercially available components. The top layer houses the analog front end on one side and the microcontroller for digital processing on the other. The bottom layer is left for the Bluetooth module and antenna.The primary design constraint while developing the device was usability (size and battery life) and signal quality of the acquired sEMG signals. Figure 1d shows the unpackaged guts of the portable unit comprising of a Bluetooth™ module (HC-06, Guangzhou HC Information Technologies Co., Ltd., China, 38mm x 17mm x 4mm) for remote data transmission; a 4-channel 24 bit analog-to-digital (A/D) conversion (ADS1294, Texas Instruments, USA, 12 mm x 12 mm x 1 mm); a rechargeable battery (PRT-13813, Sparkfun Electronics, USA, 1000 mAh, 50 mm x 34 mm x 6 mm) for on-board power supply; and a 3D-printed plastic case made of acrylonitrile butadiene styrene (ABS) for housing. The assembled unit had dimensions of 56mm x 37mm x 20mm, and weighed approximately 55g.

The custom-built, wearable device was clipped on to the user's clothing via a flexible anisotropic conductive film (ACF) wire for remote data acquisition. Signals were collected through a zero insertion force (ZIF) connector in the device. A differential input analog front end system-on-chip (SoC) (ADS1294, Texas Instrument) was used for signal conditioning and sampling of the sEMG signals and strain gauge waveforms. The SoC analog front end is specifically designed for processing bio-physical signals and incorporates a differential input, 24-bit resolution analog-to-digital converter. The SoC enables data acquisition across multiple channels at programmable resolution of up to 24 bits and sampling rate of up to 32

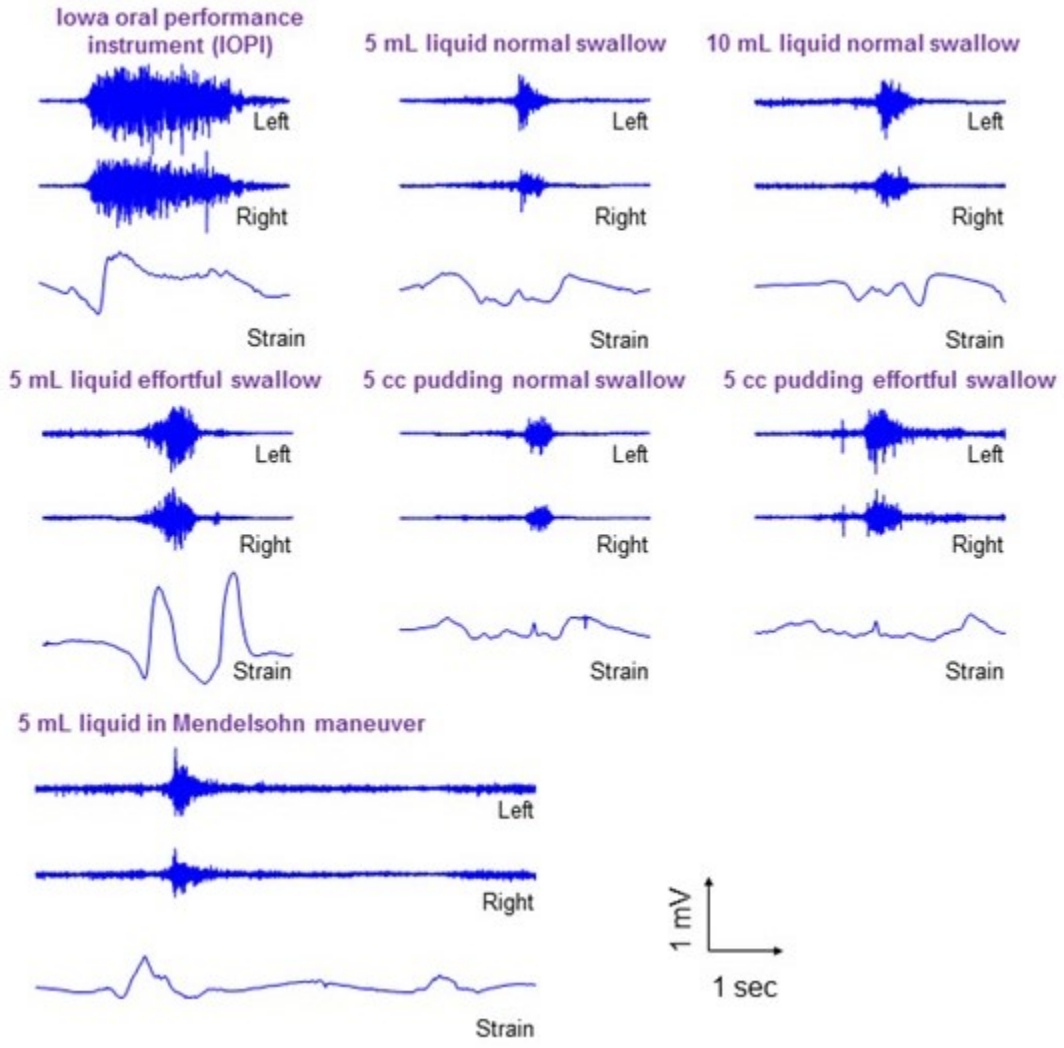

Figure 3.2. Waveforms of the sEMG and strain gauge signals obtained from the custom-built device.

ksps. The front-end circuit gain is digitally controllable to vary the resolution of the input signal. The ADC sampled the sEMG signal at a rate of 1 kHz and the strain gauge at 100Hz. The data from the SoC was collected by a Cortex-M4F microcontroller (TM4C123GH6PM, Texas Instruments) and processed with a finite impulse response, 4th order Butterworth bandpass filter with a cut-off frequency of 20-500 Hz and 0.1-20 Hz for sEMG signals and strain waveforms, respectively. The data is then transmitted via a Bluetooth™ module (HC-06, Guangzhou HC Information Technologies) to an external data acquisition system

(commercial smart tablets or phones). The signals obtained from the wearable device is shown in Fig. 3.2.

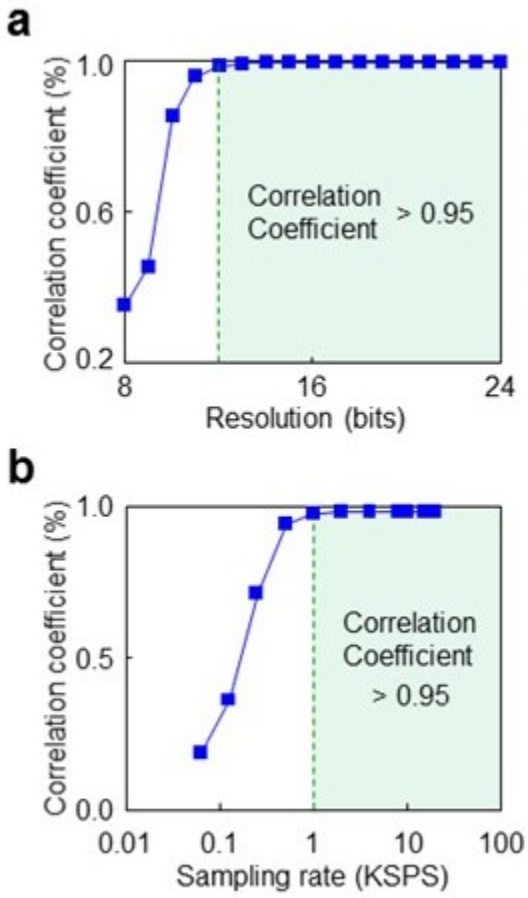

Figure 3.3. Performance characterization of the custom built built device against a commercially available gold standard (Bio Radio).

The size of the portable unit is 5.6cm × 3.8cm × 1.8cm, which is almost 3 times smaller than that of the commercial unit (10cm × 6cm × 2cm). The data acquisition front-end was programmed in terms of sampling rate and resolution to optimize between acquired signal quality and battery life. The performance characterization of device is shown in Fig. 3.3, which shows the correlation between the acquired sEMG signal and the signal obtained through a commercial device (Bio Radio). The measurements prove that a minimum sampling rate of 1 ksps (Nyquist rate) and an ADC resolution of 12 bits is more than enough to obtain a correlation coefficient >0.95. The battery life of the device was 16 hrs while

transmitting data over the Bluetooth link, which was approximately twice longer than that by using a commercial wireless unit (BioRadio).

3.2 Human Body Communication Channel Measurement

3.2.1 Introduction

The human anatomy requires wearable devices constituting a Body Area Network (BAN) to have a small form factor, thereby limiting battery capacity[29] and necessitating ultra-low-power (ULP) circuits. Communication system such as Bluetooth is a significant portion (mW) of the power-budget of such energy-constrained devices. Human body communication (HBC) promises ULP (10's of μW) BAN communication by utilizing the conductivity properties of the human body. Therefore, the power benefits similar to wire-line communication [30], [31] can be achieved while keeping the devices physically wireless.

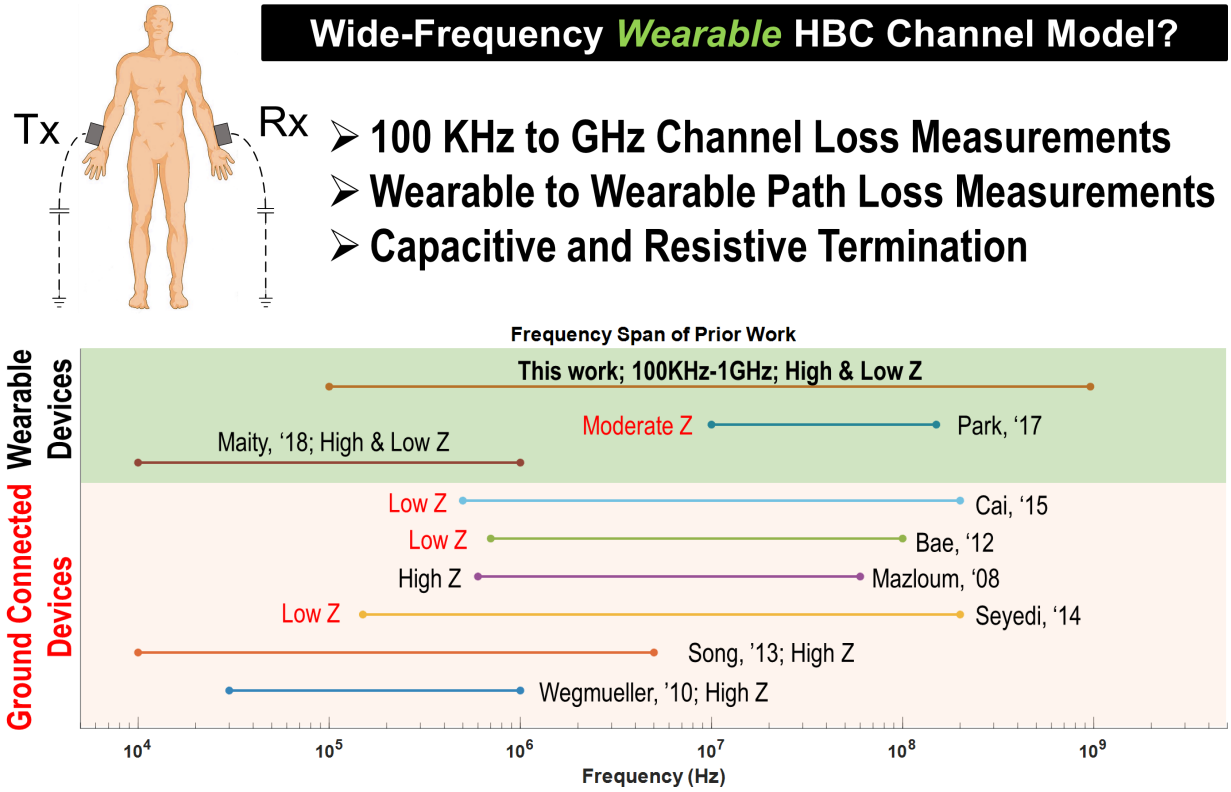

Figure 3.4. Frequency-range, termination modality and ground connection used by prior work in HBC channel measurement and the research need [32]–[38]

Capacitive HBC involves coupling and receiving the communication signal to the body through a single electrode with a floating ground electrode both at transmitter and receiver.

Only a few studies on characterizing the channel exist in literature (Fig. 3.4) on channel which are conducted in a methodical manner and cover a wide range of frequencies with different kinds of termination.

Maity[33] demonstrated that in capacitive-voltage mode HBC with high-impedance termination, the forward path contributed a path loss of only 0.5 dB, indicating that the return path capacitance primarily controls channel loss, later analyzed in-depth by Nath[39]. Traditionally, path loss measurements were made using ground connected devices such as vector network analyzers, which short the return path capacitance and grossly underestimate the path loss. Subsequently, a balun was placed between the electrodes and the measurement device to prevent this [34], [38]. Although this was a step in the right direction, the channel loss measurements were still optimistic due to large ground plane and large return path capacitance. These results obtained from large, ground connected devices are invalid for miniaturized wearable devices.

Maity developed the first Bio-Physical model [32] which established the underlying mechanism of low-frequnecy capacitive HBC as electro-quasistatic transport[31] and described the channel characteristics for various parameters like single-ended and differential electrodes, ground connected and wearable devices, among others. Although this paints a vivid picture of the channel characteristics, with both high-impedance capacitive and resistive termination, the frequency range was limited till only 1 MHz. Park [35] developed miniature wearable devices to measure channel loss from 10 MHz to 150 MHz, using moderate impedance matching networks to maximize the power transfer. This is not the optimal choice for a voltage signaling based communication, especially at low frequencies.

Maity and Park are the only studies to utilize wearable devices for channel loss measurements. However, they investigate dissimilar parameters i.e. a small span of frequency and one kind of termination. Therefore, it is imperative to present a unified set of measurements using wearable devices over wide-frequency range to help optimize HBC transceivers.

3.2.2 Bio-Physical Model

The bio-physical model proposed by Maity [32] for capacitive HBC is shown in Fig. 3.5a. The underlying mechanism for low frequencies is approximated as electro-quasistatic transport since the signal wavelength is an order of magnitude larger than the body dimension. Discounting a 5% error, this approximation is valid roughly up to 10MHz[31].

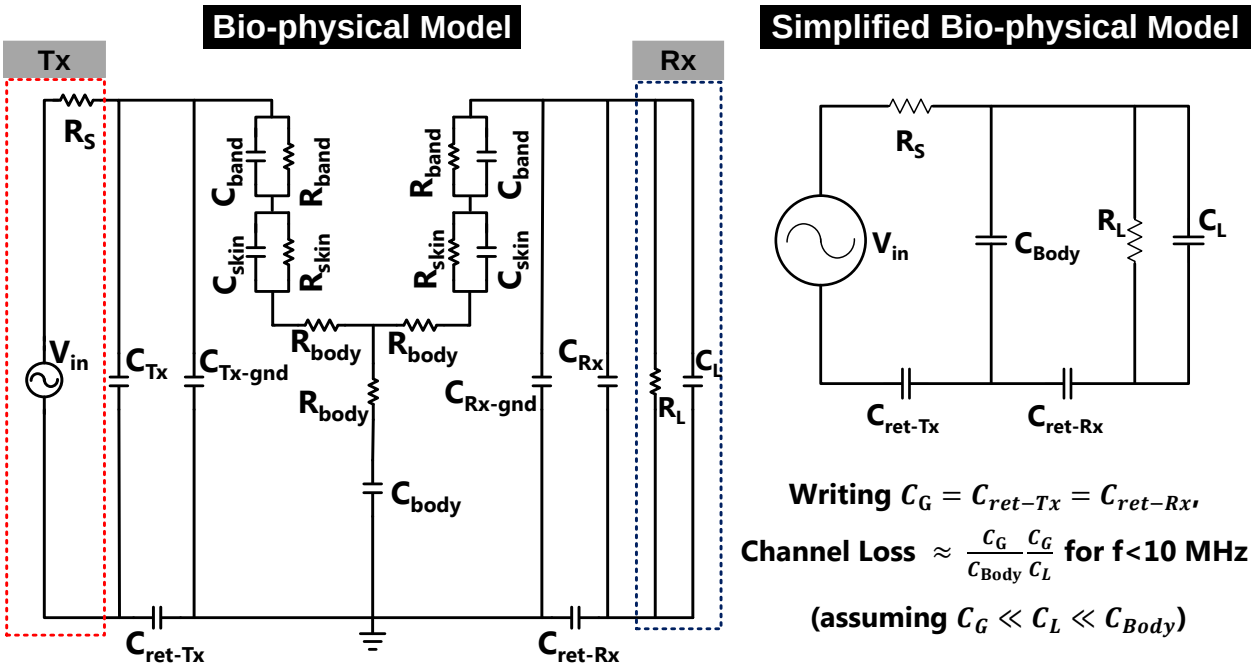

Figure 3.5. (a) Biophysical model [32]; (b) Simplified biophysical model [39].

The bio-physical model explains the various resistances and parasitic capacitance associated with HBC. The transmitter is modelled as a voltage source with a small series source impedance, whereas the receiver is modelled by its termination impedance. The return path capacitance between earth's ground and the communication devices' floating ground closes the circuit loop, allowing signal transmission. Parasitic capacitances between the earth's ground and the body, and those between the body and communication devices further affect the signal transmission and channel loss.

The return path capacitance and load capacitance primarily dictates the overall channel loss of EQS-HBC. Hence, the biophysical model coule be simplified as shown in Fig. 3.5b, [39]). The return path capacitance (C_G) could be approximated as the self-capacitance and

is proportional to the ground plane size of the transmitter and receiver[39], increasing loss for a lower (C_G) (i.e. smaller device) or a higher load capacitance (C_L). Hence, to measure channel loss for wearable devices, small form factor measurement devices must be used.

At high frequencies (beyond 10MHz), the mechanism for HBC transitions from electro-quasistatic transport to electromagnetic. As the return path capacitance will continue to play a role during this transition, a small device is still imperative for high frequency measurements. Additionally, the small size will help reduce inter-device coupling.

As shown in Fig. 3.5, the termination impedance of the receiver significantly affects channel loss in HBC. Therefore, correct termination at the receiver is of utmost importance. Previous studies [32] have shown that 50Ω termination should be avoided at low frequencies. However, as frequency increases the input impedance seen at the receiver will decrease and may eventually fall below 50Ω. It is possible that a 50Ω terminated receiver could exhibit a lower channel loss at high frequencies. Therefore the optimal termination at high frequency should be investigated in the future. Here we measure wide-frequency channel loss with wearable devices for both 50Ω and high-impedance termination (C_L).

3.2.3 Measurement Setup

Measurement Location: Anechoic Chamber

All path loss measurements are conducted inside an anechoic chamber to prevent multi-path effects and external interference from influencing the readings. The chamber has a dimension of 400x550x400 cm and the inner walls are lined with a spike-patterned foam which efficiently absorb electromagnetic waves above 80MHz. As depicted in Fig. 3.6, the human subject was placed the centre of the room to maximize distance from the side walls which are connected to earth's ground. This will minimize the change in return capacitance and accurate path loss values can be obtained.

Setup:Wearable Signal Transmitter

The entire frequency range could not be covered by a single off-the-shelf, wearable, battery powered signal generator. Therefore, two devices (Fig. 3.7a) were used as the transmitter, one for low frequency and the other for high frequency.

Low-Frequency (100KHz to 20MHz)

The EK-TM4C123GXL launchpad by Texas Instruments which highlights the TM4C123GH6PM micro-controller is used as the low frequency transmitter. It is powered by a small battery and placed in a 3D printed enclosure. The coupling electrode is made from copper tape which is fixed to an elastic band. The electrode is connected to one of the GPIO pins of the micro-controller which generates a PWM signal. The micro-controller is programmed to generate a PWM signal of 3.3V with a duty cycle of 50% between 100KHz and 20MHz. Two switches on the PCB which were programmed to cycle through the required PWM frequencies.

High-Frequency (24MHz to 960MHz)

A handheld RF signal generator (RFE6GEN) from RF Explorer is used as the transmitter for the high frequency range. The device dimension is 113x70x25 mm, and operates between 24MHz to 6GHz with a resolution of 1KHz and a frequency stability of 0.5ppm. The output signal power is 0dBm at 50Ω, with an accuracy of +/-3dB. The device body is made of aluminum and is connected to ground, therefore a layer of foam is connected below the device to prevent the body from touching the ground plane of the device.

Setup:Wearable Signal Receiver

A handheld RF spectrum analyzer (WSUB1G+) from RF Explorer is used as the wearable receiver for the entire frequency range (Fig. 3.7a). The device operates between 100KHz to 960MHz with a resolution of 0.5dB and an average noise level and amplitude accuracy of -125dB and +/-3dB, respectively. The device body is again made of aluminum and con-

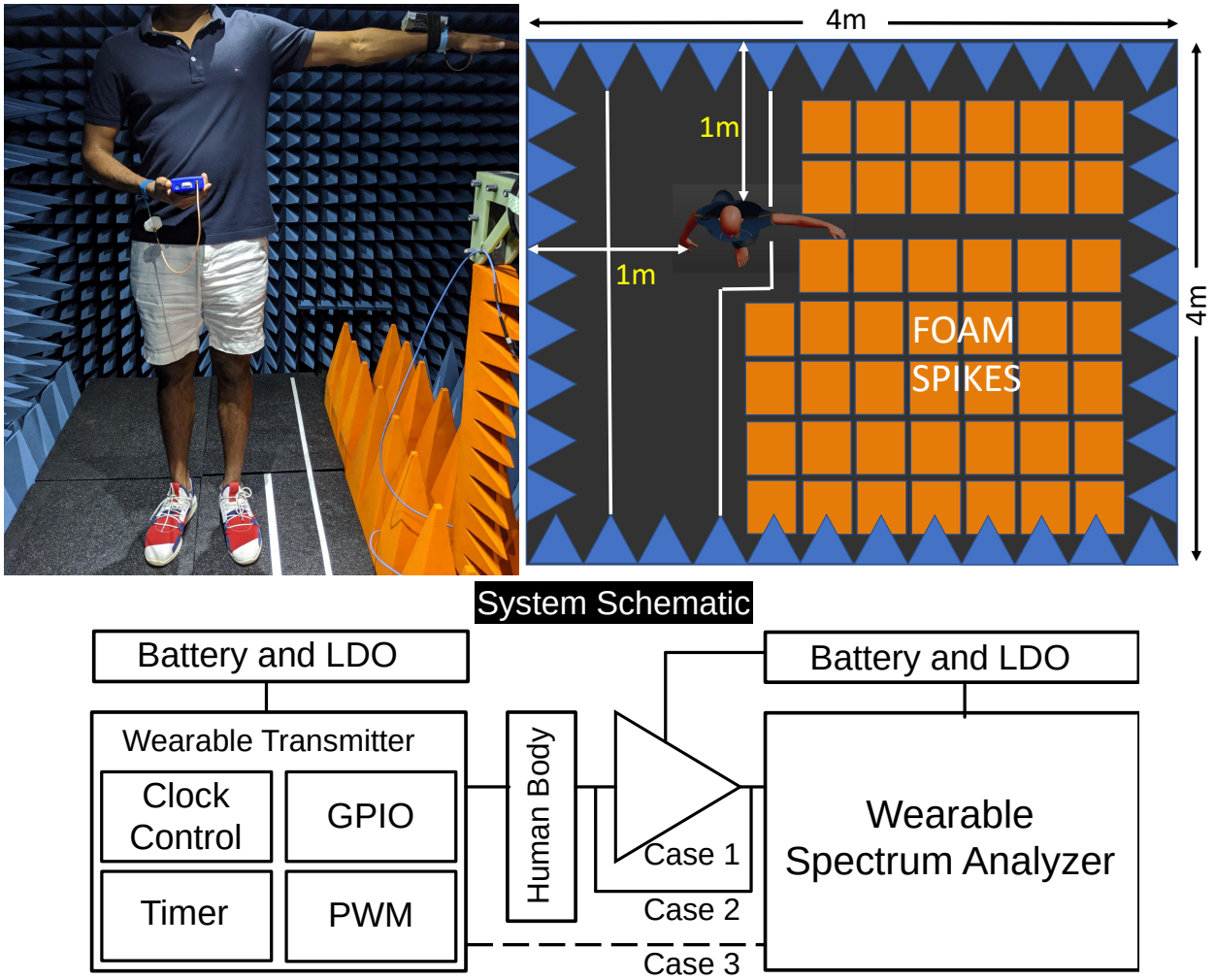

Figure 3.6. (a)Body posture for which measurements were collected; (b) Animation depicting the anechoic chamber and the physical location at which the measurements were conducted; (c) System schematic.

nected to ground, therefore the protective measures described above are used. The receiver has an input impedance of 50Ω. For low impedance termination measurements, the coupling electrode band was directly connected to the input SMA port (CASE 2 in Fig. 3.6c). For high impedance measurements, a buffer was connected (CASE 1) between the electrode and the input of the receiver.

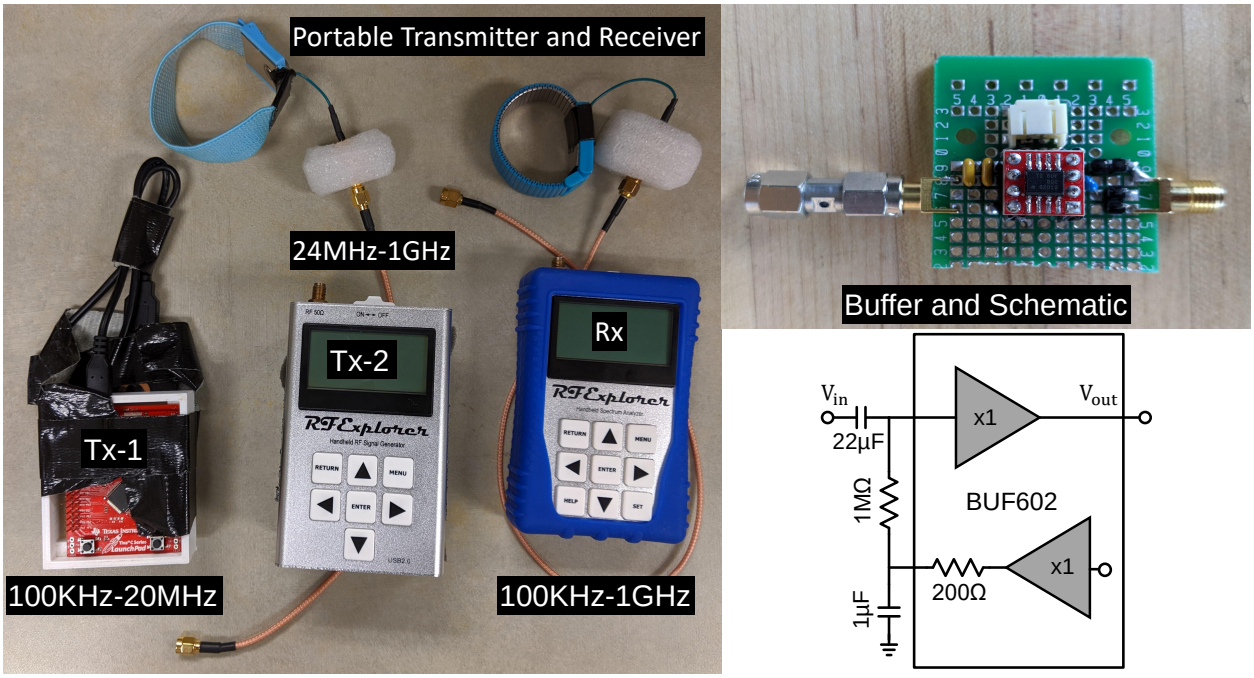

Figure 3.7. (a) Low and high frequency transmitter and receiver used for measurements; (b) High frequency buffer and schematic.

Buffer for High Impedance Termination

The high bandwidth buffer circuit was assembled on a perforated board. A high-speed buffer IC, BUF602 from Texas Instruments was used. It has a wide bandwidth of 1GHz, a slew rate of 8000V/μS, and an internal reference voltage generator, which is perfect for buffering the transmitted high-speed AC signal. The input impedance of the buffer is 1MΩ with a capacitance of 2.1pF. The input capacitance (C_L) of the complete receiver will determine the measurement and will change according to the formula shown in Fig. 3.5b.

Inter-device Coupling

Inter-device coupling measurements (CASE 3, dashed line implies no physical connection) were performed by suspending the devices inside the anechoic chamber at the exact same location as they would be if a human subject was wearing them, such that the devices see similar parasitic capacitance, making the human body as the only variable in the setup.

However, practically realizing the exact same orientation for all measurements proved to be difficult, which resulted in a high variance for inter-device coupling measurements (Fig. 3.9).

3.2.4 Measurements and Analysis

Measurement Procedure

Standardized procedure was developed and repeated, since channel loss measurements are susceptible to variations. The subject was placed at the exact same location in the anechoic chamber. The transmitter was tied to the left hand which was outstretched at shoulder, and the receiver was placed in the right hand in front of the belly. The orientation of the electrode bands were kept consistent and great care was taken to ensure a steady body posture while collecting the readings.

Due to involuntary variations in posture and placement of devices resulting from human error, fluctuations in the readings were inevitable. This was addressed by repeating the measurements multiple times over the course of a few days and averaging the results. The measurements were carried out until the standard deviation of the results dropped below 3dB. This was achieved for high frequency and low frequency channel loss measurements after 10 and 3 repetitions, respectively. Each measurement involved collecting data for both 50Ω and high impedance terminations.

High frequency measurements were carried out at 25 equally spaced points in the logarithmic scale between 24MHz and 960MHz. The transmitter was operated at power level 4, which generated a signal power between 0.1dBm and 1dBm at the fundamental frequency. Since voltage mode signaling is used in capacitive HBC, the power levels were converted to voltage before calculating channel loss. The transmitted signal power values were converted to peak voltage by, $V_{peak-Tx} = 2 * 10^{(\frac{P_{tx_{dBm}} - 10}{20})}$. The receiver recorded the input signal power at the fundamental frequency. Since the wearable spectrum analyzer has an input impedance of 50Ω, the recorded signal power can be converted to peak voltage by, $V_{peak-Rx} = 10^{(\frac{Prx_{dBm} - 10}{20})}$ and the resulting channel loss is given by, $ChannelLoss = 20 * Log_{10}(\frac{V_{peak-Rx}}{V_{peak-Tx}})$.

Low frequency measurements were carried out at 32 equally spaced points in the logarithmic scale between 100KHz and 20MHz. The peak voltage at the fundamental frequency

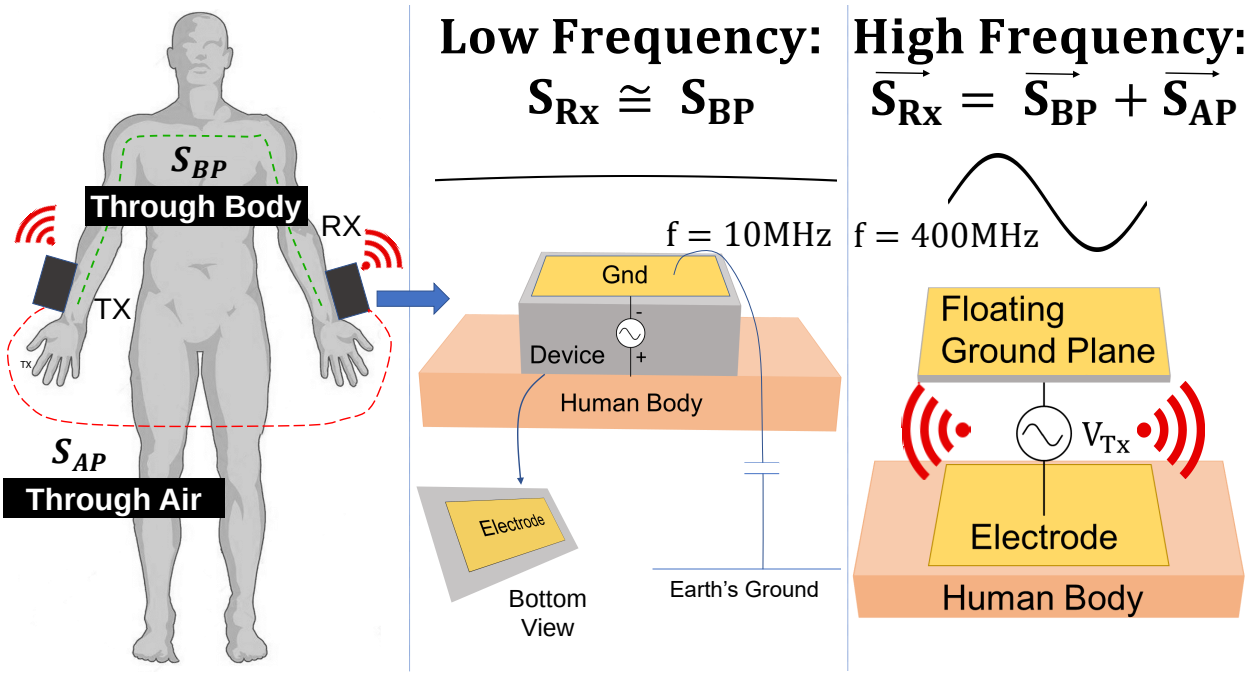

Figure 3.8. Physical path of the transmitted signal at low-frequency (mostly body) and high frequency (body and air)

of the PWM signal was calculated by computing the Fourier Transform. The peak voltage at the receiver and subsequently the channel loss was calculated as described above. For each of these frequency points the inter-device coupling readings were noted. The values below the noise floor were not plotted.

Result Analysis and Insights

The average path loss and standard deviation from 100KHz to 1GHz is depicted in Fig. 3.9. From the graph it is clearly evident that the path loss at low frequencies for 50Ω termination is more than 40dB higher (100KHz) than that for high impedance termination, which is more or less flat up to 10MHz where the difference reduces to 20dB. The flat-band loss is highly dependent on the C_L of the receiver. Beyond 10MHz, the impedance of C_L (i.e.$\frac{1}{j\omega C_L}$) starts approaching the resistive termination impedance of 50Ω. Consequently, the difference in the channel loss values reduces. The channel loss of high impedance termination can be further reduced by reducing C_L which is a function of the PCB capacitance and the

input capacitance of the buffer. In this case the chosen buffer IC and the perforated PCB used to make the circuit has resulted in a path loss of 60dB, which can be reduced by either using a thicker custom made PCB and/or a different buffer IC.

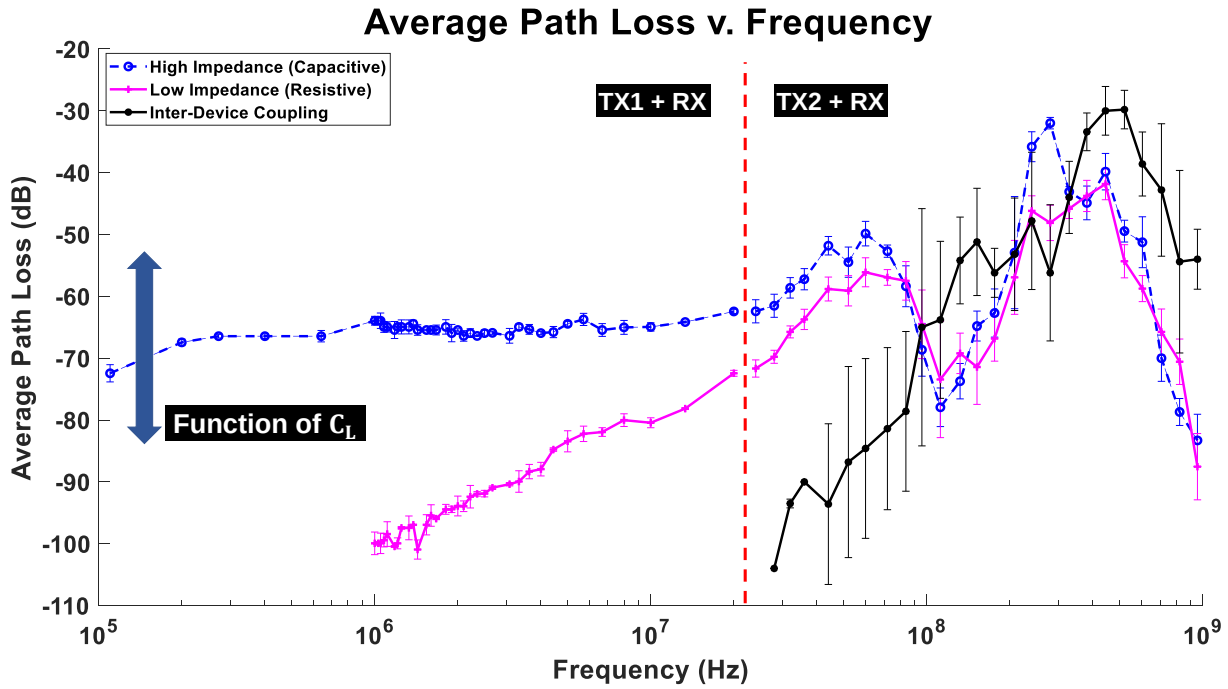

Figure 3.9. Wide-frequency Human Body Channel-loss for capacitive HBC with high impedance and resistive termination along with inter-device coupling.

Above 50-100 MHz, there is a low-pass filtering effect formed by R_S and C_L in Fig. 3.5(b). Additionally, the inter-device coupling starts to play a significant role as the dimensions of the tx/rx devices and coupling electrodes become comparable to the wavelength (Fig. 3.8). Basically, the coupler electrodes start functioning as a low-Q antenna, and a major part of the transmission takes place through direct electro-magnetic radiation between the devices, as opposed to a body-channel mode of communication. Evidently, the transmitted power peaks at about 500 MHz ($\lambda = 60$cm) which is about 4 times the device dimensions. Also, as seen in Fig. 3.9, the device-device coupling in absence of the human subject can be higher compared to the transmission when the subject is present. This further confirms that the peaking in this region happens because of line-of-sight wireless style transmission, and the human subject being in the way could hurt the transmission.

Accurately characterizing the channel for capacitive HBC at frequencies above 100MHz is in fact complicated since it's extremely difficult to isolate signal power through the body. This can be circumvented if the entire signal can be focused into the human body channel with minimal radiation. However, this is not a trivial problem since the coupling electrode band will act as an antenna. This challenge motivates future research on the design of an optimal coupler or antenna which can focus transmitted signal into the human body channel while minimizing radiation leakage and comparing the result from the above with standalone EM-radiation based coupling.

3.2.5 Conclusion

Methodical characterization of the human body channel for capacitive HBC using miniaturized wearable devices across a wide 4-decade frequency range with various types of termination is presented, which aims to fill the void in literature and serve as the backbone for the emerging field of HBC. The results have shown that channel loss is significantly higher at low frequencies for a 50Ω termination as compared to high impedance termination. The difference steadily decreases beyond 10MHz and beyond 100MHz, inter-device coupling dominates and an accurate measurement of only human-body portion of the channel loss is hard to obtain. This motivates future research on optimizing the electrode coupler and device design to ensure that the transmitted signal is directed into the human body with minimal radiation leakage for comparison as well as optimal BAN antenna/coupler design purposes.

3.3 Animal Body Communication Device

3.3.1 Introduction

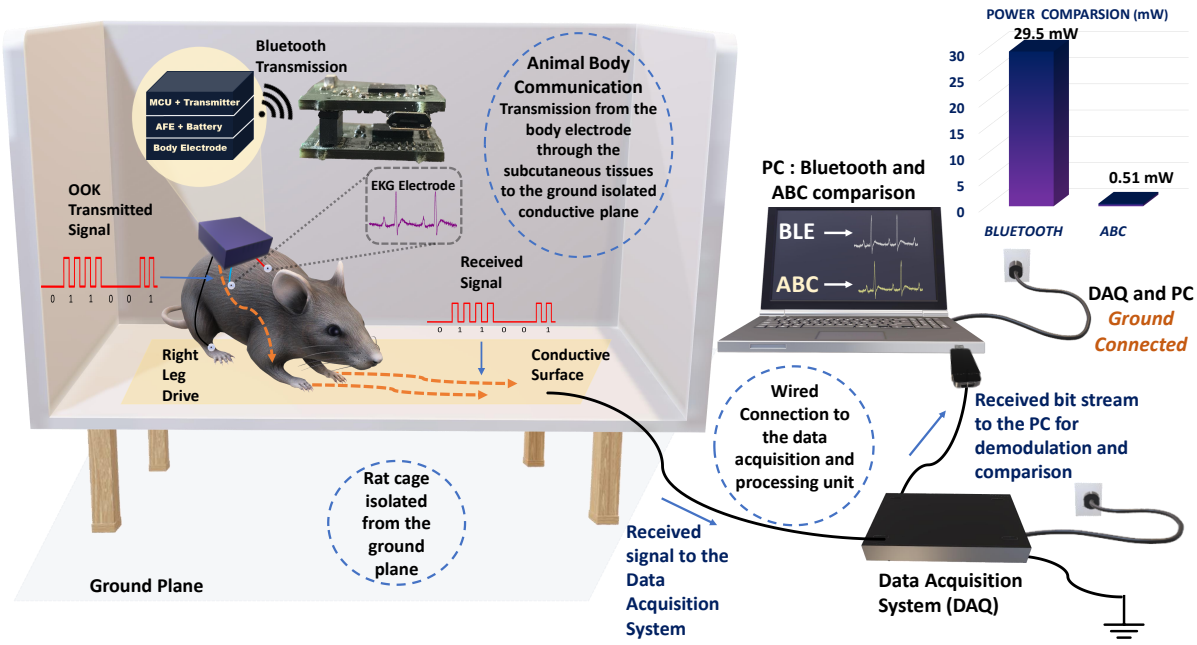

Figure 3.10. Animal Body Communication: a) Overview of Animal Body Communication on a Rodent Model. Custom designed sensor node is placed on the back of the rat. This sensor node is capable of sensing and transmitting the surface biopotential signals via Bluetooth and Animal Body Communication. The sensed signal is transmitted through the body to the conductive surface in the form of OOK (On-Off Keying) sequences. The specially designed rat cage is isolated from the ground surface. A conductive surface is placed on the base of the rat cage which is then connected to a Data Acquisition System (DAQ) which receives the transmitted signals. The Bluetooth receiver and DAQ are connected to a PC for processing, with the DAQ and PC ground referenced. In this model Bluetooth communication acts as a validity check for ABC. *The rat model in a) was created using Paint 3D.*

Continuous recording of bio-potential signals through small form-factor wearable devices has enabled a better understanding of physiology, preventative healthcare, and enhanced therapeutic treatments as shown in Section 3.1. These small form-factor wireless devices consume large amounts of power since radio-frequency communication is used which is inherently lossy and requires up-conversion of the base-band signal. Consequently, either large

battery packs, frequent recharging or large energy harvesters are required to achieve a long device lifetime. To overcome these constraints human body communication can be employed for significant improvements to the size, weight, area, and power benefits of the wearable devices as compared to conventional electromagnetic communication systems.

Animals have been used for hundreds of years to conduct research in medicine and medical devices due to their anatomy and physiology being similar to the human body. Therefore, it serves as an ideal starting point to prove the efficacy and reliability of communicating information through the body as the communication modality while simultaneously recording bio-potential signals in a controlled environment. Animal Body Communication (ABC) will also address a research need in animal sciences wherein wherein wearable, untethered, small, light-weight monitoring devices are required to minimally influence the animals behaviour for more accurate studies. ABC is demonstrated with a sub-inch^3, custom-designed sensor node. Figure 3.10, describes the concept of the ABC setup, surface biopotential signals are acquired by a custom-designed sensor node that then transmits the signal using ABC through the subcutaneous tissues of the animal body using EQS-ABC. These signals are picked up by a receiver connected to the ground isolated conductive surface. In this setup, we also transmit the signals using Bluetooth as a method to compare the ABC transmitted signal with an established communication modality. The low power requirement enables the use of smaller batteries or coils in the case of energy harvested nodes. Experiments were performed with EKG signals of the rat as the chosen surface biopotential signal. This device serves as the first demonstration of animal body communication.

3.3.2 System Architecture

Size, weight, area, and power consumption of wireless recording devices have the potential to significantly affect animal behavior and compromise the quality and length of recordings, thereby hindering scientific studies. Overcoming these obstacles formed the core design objectives for the custom node for the acquisition of biopotential signals and wireless transmission of data and resulted in the following initial specifications. Physical dimensions were constrained to one cubic inch, which is sufficiently small to be placed on a rodent and

large enough to house the various components. The net weight and power consumption were capped at 50g, and 50 mW respectively. This posed a significant challenge since the analog front end for sensing, micro-controller for computing, wireless communication for comparison purposes, power management, and animal body communication had to be miniaturized and integrated into the device while meeting the power budget.

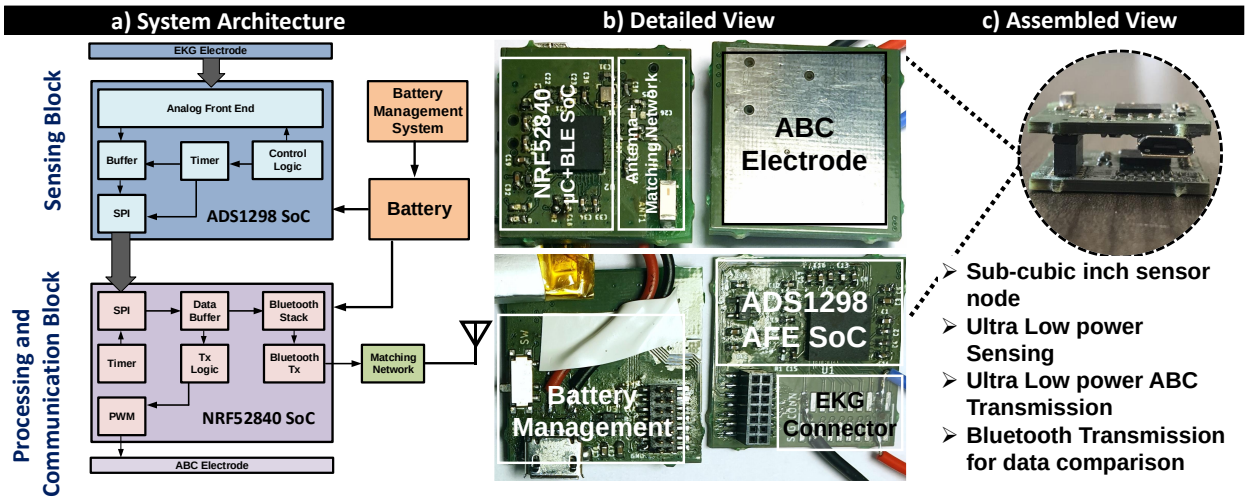

Figure 3.11. System Architecture of the custom-built node for biopotential acquisition through animal body communication and Bluetooth Low Energy; a) Block diagram of the custom-built node, b) Functional blocks depicted on the actual device, c) Custom node after stacking.

The system architecture as shown in Figure 3.11**a** can be broadly divided into three blocks, the custom-wireless signal acquisition node, the Bluetooth receiver connected to the data logging system (computer), and the animal body communication receiver. The custom node consisted of two vertically stacked custom-designed printed circuit boards (PCB) which were populated with commercially available integrated circuits and discrete components. The top board in the stack contained the micro-controller and Bluetooth System on Chip (SoC), along with the antenna and matching network on the top layer. The bottom layer consisted of the power management system and charging connector. The analog front end was housed on the top layer of the bottom stack, with the bottom layer serving as the electrode for animal body communication. The detailed view and the assembled view of the sensor node is shown in as shown in Figure 3.11**b** and 3.11**c** respectively.

A System on Chip (NRF52840, Nordic Semiconductors) which integrates an ARM Cortex-M4F micro-controller and a Bluetooth 5.0 transceiver was selected to form the core of the node since it would minimize the device footprint and power consumption. The on board 1MB flash memory and 256KB RAM was sufficiently large to store the sampled signals and implement in-sensor analytics in the future. Power efficiency was further improved by utilizing the on-chip DC-DC converters.

The custom node collected the EKG signals from a zero-insertion force connector placed on the PCB. Signal conditioning and sampling of the EKG signal was performed by another SoC (ADS1298, Texas Instruments). This analog front-end chip incorporates a programmable gain differential amplifier and right-leg drive generation for conditioning EKG signals, which were subsequently sampled at 500Hz by a 24-bit analog to digital converter. The SoC was programmed to optimize signal acquisition quality and power consumption. The sampled signals were sent to the micro-controller through an on-chip Serial Peripheral Interface.

The sampled data was stored in a buffer in the micro-controller until the transmission window started. The samples were then converted to characters and transmitted as a string over Bluetooth after adding delimiters to differentiate between subsequent samples. For Animal Body Communication, the sample was transmitted in its original 24-bit binary integer form after creating packets by adding two bits (binary 1) at the start and end of the sample. Each bit in ABC was represented by on-off keying, wherein a 500kHz, 50% duty cycle square wave was turned on (binary 1) or off (binary 0). ABC data was transmitted at 25Kbps, which was significantly lower than the minimum required Bluetooth bandwidth of 45Kbps, which excludes the overhead added by the Bluetooth stack.

The custom-designed node was packaged in a 3D-printed housing of dimensions 25mm x 25mm x 10mm, which is equivalent to 0.39 cubic inches. It had a net weight of 20g and average power consumption of 28.5 mW (with Bluetooth transmission for data comparison purposes) which resulted in approximately 20 hours of battery life. This is 19 times smaller and has more than twice the battery life when compared to a commercial wireless unit (Bio-Radio). We expect a much longer lifetime when the Bluetooth transmission is turned off and only ABC transmission is turned on. The power required for sensing is typically orders

of magnitude lower than the power required for communication, thus the system power is dominated by this communication power. The ABC transmission power is 50x lower when compared to the Bluetooth transmission power and this translates into an order of magnitude improvement in the device lifetime and reduction in the battery size.

The Bluetooth receiver was essentially another NRF52840 SoC connected via USB to the data logging system, which in this case was a computer. This setup was used instead of the inbuilt Bluetooth device of the computer since it would be easier to collate data from multiple transmitters.

The conductive signal plane is connected to the high impedance receiver probe. A computer-based oscilloscope, by Pico Technologies, was used as the ABC receiver. The OOK sequences are sampled at 3.9 MSamples/s and collected for post-processing.

3.3.3 Signal Processing

OOK sequences collected from the ABC receiver are sent to a computer for processing. Signals are first band-passed between 400kHz to 600 kHz with 80 dB attenuation software filters. Filtered sequences are demodulated using envelop detection and thresholding. Sequences are then decoded using the start and stop bit followed by software error correction. Bluetooth sequences in the form of ADC codes are converted to corresponding voltage values and compared to the received ABC signals.

3.3.4 Communication Protocols

Time Multiplexed Data:

As discussed earlier, a requisite for animal body communication especially while recording surface biopotential signals is the need to time multiplex the sensing and transmission periods.

Error-Correcting Algorithms:

There is a possibility to bring in redundancy into the communication channel to ensure the robustness of this communication modality. We have shown that if the rat foot is lifted from the conductive surface, the received signal can still be picked up by the receiver. The goal of

this paper is to ensure that long term recordings of freely moving animals can be obtained. To ensure that there is a successful transmission of data, error-correcting algorithms become a necessity.

Bi-modular Redundancy can be introduced by repeating packets over time. In the event of a jump or signal drop, repeated packets ensure that the signal information is faithfully transmitted. This technique reduces the data rate due to the added redundancy.

Block Codes a common error-correcting technique of encoding the data in blocks, such that the code is a linear combination of the message and parity bits in a linear block code.

3.3.5 Conclusion

To conclude, a custom-designed sensor node was designed to acquire bio-potential signals from a rat and transmit it through the animals body. Bluetooth was used as the communication gold-standard to validate animal body communication. During the course of testing the data received from both modalities had a correlation coefficient > 0.99 at all times. However, there was a stark difference in power consumption since ABC consumed 0.5mW of power as compared to 29.5mW for Bluetooth transmission. Although a $> 50x$ reduction in power consumption is significant, it can be further reduced if a custom-designed IC integrates ABC with the analog front end and computing. It was also demonstrated that reliable signals could be received from the rat even when the foot was raised or in improper contact with the receiver. While this device was built for capturing EKG signals, it can be extended to any bio-potential signal where low power communication modalities are essential, such as neural signal acquisition and transmission. Therefore, electro-quasistatic animal body communication can prove to be the next advancement in communication for animal studies and by extension wearble devices for humans by enabling ultra-low power and efficient communication.

REFERENCES

[1] *VNI Forecast Highlights Tool*, [Online]. Available: https://www.cisco.com/c/m/en_us/solutions/service-provider/vni-forecast-highlights.html, [Accessed: Jan-30-2020].

[2] A. Mainwaring, D. Culler, J. Polastre, R. Szewczyk, and J. Anderson, "Wireless sensor networks for habitat monitoring," in *Proceedings of the 1st ACM International Workshop on Wireless Sensor Networks and Applications*, New York, NY, USA: Association for Computing Machinery, 2002, ISBN: 1581135890. DOI: 10.1145/570738.570751. [Online]. Available: https://doi.org/10.1145/570738.570751.

[3] G. Werner-Allen, K. Lorincz, M. Ruiz, O. Marcillo, J. Johnson, J. Lees, and M. Welsh, "Deploying a wireless sensor network on an active volcano," *IEEE Internet Computing*, vol. 10, no. 2, pp. 18–25, 2006. DOI: 10.1109/MIC.2006.26.

[4] K. Chebrolu, B. Raman, N. Mishra, P. K. Valiveti, and R. Kumar, "Brimon: A sensor network system for railway bridge monitoring," in *Proceedings of the 6th International Conference on Mobile Systems, Applications, and Services*, New York, NY, USA: Association for Computing Machinery, 2008, ISBN: 9781605581392. DOI: 10.1145/1378600.1378603. [Online]. Available: https://doi.org/10.1145/1378600.1378603.

[5] B. Chatterjee, D. .-.-H. Seo, S. Chakraborty, S. Avlani, X. Jiang, H. Zhang, M. Abdallah, N. Raghunathan, C. Mousoulis, A. Shakouri, S. Bagchi, D. Peroulis, and S. Sen, "Context-aware collaborative intelligence with spatio-temporal in-sensor-analytics for efficient communication in a large-area iot testbed," *IEEE Internet of Things Journal*, pp. 1–1, 2020. DOI: 10.1109/JIOT.2020.3036087.

[6] S. Sudevalayam and P. Kulkarni, "Energy harvesting sensor nodes: Survey and implications," *IEEE Communications Surveys Tutorials*, vol. 13, no. 3, pp. 443–461, 2011. DOI: 10.1109/SURV.2011.060710.00094.

[7] T. Karnik et al., "A cm-scale self-powered intelligent and secure iot edge mote featuring an ultra-low-power soc in 14nm tri-gate cmos," in *2018 IEEE International Solid - State Circuits Conference - (ISSCC)*, Feb. 2018, pp. 46–48. DOI: 10.1109/ISSCC.2018.8310176.

[8] Y. K. Tan and S. K. Panda, "Optimized wind energy harvesting system using resistance emulator and active rectifier for wireless sensor nodes," *IEEE Transactions on Power Electronics*, vol. 26, no. 1, pp. 38–50, 2011. DOI: 10.1109/TPEL.2010.2056700.

[9] W. Lee, M. J. W. Schubert, B. Ooi, and S. J. Ho, "Multi-source energy harvesting and storage for floating wireless sensor network nodes with long range communication capability," *IEEE Transactions on Industry Applications*, vol. 54, no. 3, pp. 2606–2615, 2018. DOI: 10.1109/TIA.2018.2799158.

[10] Z. Stamenkovic, M. Mabon, M. Gautier, B. Vrigneau, M. Le Gentil, and O. Berder, "The smaller the better: Designing solar energy harvesting sensor nodes for long-range monitoring," *Wireless Communications and Mobile Computing*, vol. 2019, p. 11, 2019. DOI: 10.1155/2019/2878545.

[11] J. Zhang, P. Li, Y. Wen, F. Zhang, and C. Yang, "A management circuit with upconversion oscillation technology for electric-field energy harvesting," *IEEE Transactions on Power Electronics*, vol. 31, no. 8, pp. 5515–5523, 2016. DOI: 10.1109/TPEL.2015.2491960.

[12] N. Kong and D. S. Ha, "Low-power design of a self-powered piezoelectric energy harvesting system with maximum power point tracking," *IEEE Transactions on Power Electronics*, vol. 27, no. 5, pp. 2298–2308, 2012. DOI: 10.1109/TPEL.2011.2172960.

[13] C. Alippi and C. Galperti, "An adaptive system for optimal solar energy harvesting in wireless sensor network nodes," *IEEE Transactions on Circuits and Systems I: Regular Papers*, vol. 55, no. 6, pp. 1742–1750, 2008. DOI: 10.1109/TCSI.2008.922023.

[14] T. Ruan, Z. J. Chew, and M. Zhu, "Energy-aware approaches for energy harvesting powered wireless sensor nodes," *IEEE Sensors Journal*, vol. 17, no. 7, pp. 2165–2173, 2017. DOI: 10.1109/JSEN.2017.2665680.

[15] J. Recas Piorno, C. Bergonzini, D. Atienza, and T. Simunic Rosing, "Prediction and management in energy harvested wireless sensor nodes," in *2009 1st International Conference on Wireless Communication, Vehicular Technology, Information Theory and*

Aerospace Electronic Systems Technology, 2009, pp. 6–10. DOI: 10.1109/WIRELESSVITAE.2009.5172412.

[16] *CC1352R Product Specs*, [Online]. Available: https://www.ti.com/lit/ds/symlink/cc1352r.pdf?ts=1616415713151, [Accessed: Sep-14-2020].

[17] N. Jaziri, A. Boughamoura, J. Müller, B. Mezghani, F. Tounsi, and M. Ismail, "A comprehensive review of thermoelectric generators: Technologies and common applications," *Energy Reports*, vol. 6, pp. 264–287, 2020, ISSN: 2352-4847. DOI: https://doi.org/10.1016/j.egyr.2019.12.011. [Online]. Available: https://www.sciencedirect.com/science/article/pii/S2352484719306997.

[18] V. Kuhn, C. Lahuec, F. Seguin, and C. Person, "A multi-band stacked rf energy harvester with rf-to-dc efficiency up to 84%," *IEEE Transactions on Microwave Theory and Techniques*, vol. 63, no. 5, pp. 1768–1778, 2015. DOI: 10.1109/TMTT.2015.2416233.

[19] M. A. Green, K. Emery, Y. Hishikawa, W. Warta, E. D. Dunlop, D. H. Levi, and A. W. Y. Ho-Baillie, "Solar cell efficiency tables (version 49)," *Progress in Photovoltaics*, vol. 25, no. 1, Nov. 2016. DOI: 10.1002/pip.2855.

[20] A. H. Sparks, "Nasapower: A nasa power global meteorology, surface solar energy and climatology data client for r," *The Journal of Open Source Software*, vol. 3, no. 30, p. 1035, Oct. 2018. DOI: 10.21105/joss.01035.

[21] B. Chatterjee, P. Panda, S. Maity, A. Biswas, K. Roy, and S. Sen, "Exploiting inherent error resiliency of deep neural networks to achieve extreme energy efficiency through mixed-signal neurons," *IEEE Transactions on Very Large Scale Integration (VLSI) Systems*, vol. 27, no. 6, pp. 1365–1377, Jun. 2019.

[22] C. H. Bennett, "Notes on landauer's principle, reversible computation, and maxwell's demon," *Studies in History and Philosophy of Science Part B: Studies in History and Philosophy of Modern Physics*, vol. 34, no. 3, pp. 501–510, 2003, Quantum Information and Computation, ISSN: 1355-2198. DOI: https://doi.org/10.1016/S1355-2198(03)00039-X. [Online]. Available: http://www.sciencedirect.com/science/article/pii/S135521980300039X.

[23] H. T. Friis, "A Note on a Simple Transmission Formula," *Proceedings of the IRE*, vol. 34, no. 5, pp. 254–256, May 1946, ISSN: 0096-8390. DOI: 10.1109/JRPROC.1946.234568.

[24] A. J. Johansson, "Performance of a radio link between a base station and a medical implant utilising the MICS standard," in *The 26th Annual International Conference of the IEEE Engineering in Medicine and Biology Society*, vol. 1, Sep. 2004, pp. 2113–2116.

[25] B. Chatterjee, N. Cao, A. Raychowdhury, and S. Sen, "Context-aware intelligence in resource-constrained iot nodes: Opportunities and challenges," *IEEE Design Test*, vol. 36, no. 2, pp. 7–40, Apr. 2019.

[26] A. Ebrazeh and P. Mohseni, "30 pJ/b, 67 Mbps, Centimeter-to-Meter Range Data Telemetry With an IR-UWB Wireless Link," *IEEE Transactions on Biomedical Circuits and Systems*, vol. 9, no. 3, pp. 362–369, Jun. 2015, ISSN: 1932-4545.

[27] S. Paul et al., "An energy harvesting wireless sensor node for iot systems featuring a near-threshold voltage ia-32 microcontroller in 14nm tri-gate cmos," in *2016 IEEE Symposium on VLSI Circuits (VLSI-Circuits)*, Jun. 2016, pp. 1–2. DOI: 10.1109/VLSIC.2016.7573485.

[28] M. K. Kim, C. Kantarcigil, B. Kim, R. K. Baruah, S. Maity, Y. Park, K. Kim, S. Lee, J. B. Malandraki, S. Avlani, A. Smith, S. Sen, M. A. Alam, G. Malandraki, and C. H. Lee, "Flexible submental sensor patch with remote monitoring controls for management of oropharyngeal swallowing disorders," *Science Advances*, vol. 5, no. 12, 2019. DOI: 10.1126/sciadv.aay3210. eprint: https://advances.sciencemag.org/content/5/12/eaay3210.full.pdf. [Online]. Available: https://advances.sciencemag.org/content/5/12/eaay3210.

[29] B. Chatterjee *et al.*, "Context-aware intelligence in resource-constrained iot nodes: Opportunities and challenges," *IEEE Design & Test*, vol. 36, no. 2, pp. 7–40, 2019.

[30] S. Maity *et al.*, "Bodywire: A 6.3-pj/b 30-mb/s- 30-db sir-tolerant broadband interference-robust human body communication transceiver using time domain interference rejection," *IEEE Journal of Solid-State Circuits*, vol. 54, no. 10, pp. 2892–2906, 2019.

[31] D. Das *et al.*, "Enabling covert body area network using electro-quasistatic human body communication," *Scientific reports*, vol. 9, no. 1, p. 4160, 2019.

[32] S. Maity *et al.*, *Bio-physical modeling, characterization, and optimization of electro-quasistatic human body communication*, Jun. 2019. DOI: 10.1109/TBME.2018.2879462.

[33] S. Maity *et al.*, "Characterization of Human Body Forward Path Loss and Variability Effects in Voltage-Mode HBC," *IEEE Microwave and Wireless Components Letters*, vol. 28, no. 3, pp. 266–268, Mar. 2018, ISSN: 1531-1309. DOI: 10.1109/LMWC.2018.2800529.

[34] M. H. Sayedi *et al.*, *A novel intrabody communication transceiver for biomedical applications*, Victoria University, Footscray, VIC, Australia, 2014.

[35] J. Park *et al.*, "Channel Modeling of Miniaturized Battery-Powered Capacitive Human Body Communication Systems," *IEEE Transactions on Biomedical Engineering*, vol. 64, no. 2, pp. 452–462, Feb. 2017, ISSN: 0018-9294. DOI: 10.1109/TBME.2016.2560881.

[36] M. S. Wegmueller *et al.*, "Signal Transmission by Galvanic Coupling Through the Human Body," *IEEE Transactions on Instrumentation and Measurement*, vol. 59, no. 4, pp. 963–969, Apr. 2010, ISSN: 0018-9456. DOI: 10.1109/TIM.2009.2031449.

[37] Y. Song *et al.*, "Review of the Modeling, Simulation and Implement of Intra-body Communication," *Defence Technology*, vol. 9, no. 1, pp. 10–17, Mar. 2013, ISSN: 2214-9147. DOI: 10.1016/j.dt.2013.10.001. [Online]. Available: http://www.sciencedirect.com/science/article/pii/S2214914713000238.

[38] J. Bae *et al.*, "The signal transmission mechanism on the surface of human body for body channel communication," *IEEE Transactions on Microwave Theory and Techniques*, vol. 60, no. 3, pp. 582–593, 2012, ISSN: 1557-9670. DOI: 10.1109/TMTT.2011.2178857.

[39] M. Nath *et al.*, "Towards understanding the return path capacitance in capacitive human body communication," *IEEE Transactions on Circuits and Systems II: Express Briefs*, pp. 1–1, 2019, ISSN: 1558-3791. DOI: 10.1109/TCSII.2019.2953682.

[40] S. Sen, "Socialhbc: Social networking and secure authentication using interference-robust human body communication," in *Proceedings of the 2016 International Symposium on Low Power Electronics and Design*, ser. ISLPED '16, San Francisco Airport, CA, USA: Association for Computing Machinery, 2016, pp. 34–39, ISBN: 9781450341851. DOI: 10.1145/2934583.2934609. [Online]. Available: https://doi.org/10.1145/2934583.2934609.

[41] S. Maity, D. Das, X. Jiang, and S. Sen, "Secure human-internet using dynamic human body communication," in *2017 IEEE/ACM International Symposium on Low Power Electronics and Design (ISLPED)*, 2017, pp. 1–6. DOI: 10.1109/ISLPED.2017.8009190.

[42] S. Maity, D. Das, and S. Sen, "Wearable health monitoring using capacitive voltage-mode human body communication," in *2017 39th Annual International Conference of the IEEE Engineering in Medicine and Biology Society (EMBC)*, 2017, pp. 1–4. DOI: 10.1109/EMBC.2017.8036748.

[43] S. Maity, D. Das, and S. Sen, "Adaptive interference rejection in human body communication using variable duty cycle integrating ddr receiver," in *Design, Automation Test in Europe Conference Exhibition (DATE), 2017*, 2017, pp. 1763–1768. DOI: 10.23919/DATE.2017.7927278.

[44] S. Maity, P. Mehrotra, and S. Sen, "An improved update rate baud rate cdr for integrating human body communication receiver," in *2018 IEEE Biomedical Circuits and Systems Conference (BioCAS)*, 2018, pp. 1–4. DOI: 10.1109/BIOCAS.2018.8584820.

[45] S. Maity, D. Yang, B. Chatterjee, and S. Sen, "A sub-nw wake-up receiver for human body communication," in *2018 IEEE Biomedical Circuits and Systems Conference (BioCAS)*, 2018, pp. 1–4. DOI: 10.1109/BIOCAS.2018.8584785.

[46] S. Maity, D. Das, B. Chatterjee, and S. Sen, "Characterization and classification of human body channel as a function of excitation and termination modalities," in *2018*

40th Annual International Conference of the IEEE Engineering in Medicine and Biology Society (EMBC), 2018, pp. 3754–3757. DOI: 10.1109/EMBC.2018.8513332.

[47] D. Das, S. Maity, B. Chatterjee, and S. Sen, "In-field remote fingerprint authentication using human body communication and on-hub analytics," in *2018 40th Annual International Conference of the IEEE Engineering in Medicine and Biology Society (EMBC)*, 2018, pp. 5398–5401. DOI: 10.1109/EMBC.2018.8513667.

[48] M. Nath, S. Maity, and S. Sen, "Toward understanding the return path capacitance in capacitive human body communication," *IEEE Transactions on Circuits and Systems II: Express Briefs*, vol. 67, no. 10, pp. 1879–1883, 2020. DOI: 10.1109/TCSII.2019.2953682.

[49] P. Mehrotra, S. Maity, and S. Sen, "An improved update rate cdr for interference robust broadband human body communication receiver," *IEEE Transactions on Biomedical Circuits and Systems*, vol. 13, no. 5, pp. 868–879, 2019. DOI: 10.1109/TBCAS.2019.2940746.

[50] S. Maity, X. Jiang, and S. Sen, "Theoretical analysis of am and fm interference robustness of integrating ddr receiver for human body communication," *IEEE Transactions on Biomedical Circuits and Systems*, vol. 13, no. 3, pp. 566–578, 2019. DOI: 10.1109/TBCAS.2019.2911475.

[51] D. Das, S. Maity, B. Chatterjee, and S. Sen, "Enabling covert body area network using electro-quasistatic human body communication," *Scientific Reports*, vol. 9, no. 4160, 2019. DOI: 10.1038/s41598-018-38303-x.

[52] S. Maity, D. Yang, S. S. Redford, D. Das, B. Chatterjee, and S. Sen, "Bodywire-hci: Enabling new interaction modalities by communicating strictly during touch using electro-quasistatic human body communication," vol. 27, no. 6, Nov. 2020, ISSN: 1073-0516. DOI: 10.1145/3406238. [Online]. Available: https://doi.org/10.1145/3406238.

[53] S. Maity, M. Nath, G. Bhattacharya, B. Chatterjee, and S. Sen, "On the safety of human body communication," *IEEE Transactions on Biomedical Engineering*, vol. 67, no. 12, pp. 3392–3402, 2020. DOI: 10.1109/TBME.2020.2986464.

[54] B. Chatterjee, A. Srivastava, D.-H. Seo, D. Yang, and S. Sen, "A context-aware reconfigurable transmitter with 2.24 pj/bit, 802.15.6 nb-hbc and 4.93 pj/bit, 400.9 mhz medradio modes with 33.6% transmit efficiency," in *2020 IEEE Radio Frequency Integrated Circuits Symposium (RFIC)*, 2020, pp. 75–78. DOI: 10.1109/RFIC49505.2020.9218344.

[55] S. Maity, N. Modak, D. Yang, S. Avlani, M. Nath, J. Danial, D. Das, P. Mehrotra, and S. Sen, "A 415 nw physically and mathematically secure electro-quasistatic hbc node in 65nm cmos for authentication and medical applications," in *2020 IEEE Custom Integrated Circuits Conference (CICC)*, 2020, pp. 1–4. DOI: 10.1109/CICC48029.2020.9075930.

[56] S. Avlani, M. Nath, S. Maity, and S. Sen, "A 100khz-1ghz termination-dependent human body communication channel measurement using miniaturized wearable devices," in *2020 Design, Automation Test in Europe Conference Exhibition (DATE)*, 2020, pp. 650–653. DOI: 10.23919/DATE48585.2020.9116556.

[57] S. Sen, S. Maity, and D. Das, "The body is the network: To safeguard sensitive data, turn flesh and tissue into a secure wireless channel," *IEEE Spectr.*, vol. 57, no. 12, pp. 44–49, Dec. 2020, ISSN: 0018-9235. DOI: 10.1109/MSPEC.2020.9271808. [Online]. Available: https://doi.org/10.1109/MSPEC.2020.9271808.

[58] A. Datta, M. Nath, D. Yang, and S. Sen, "Advanced biophysical model to capture channel variability for eqs capacitive hbc," *IEEE Transactions on Biomedical Engineering*, pp. 1–1, 2021. DOI: 10.1109/TBME.2021.3074138.

[59] M. Nath, A. K. Ulvog, S. Weigand, and S. Sen, *Understanding the role of magnetic and magneto-quasistatic fields in human body communication*, 2020. arXiv: 2011.00125 [eess.SP].

[60] N. Modak, D. Das, M. Nath, B. Chatterjee, K. Gaurav Kumar, S. Maity, and S. Sen, "A 65nm resonant electro-quasistatic 5-240uw human whole-body powering and 2.19uw communication soc with automatic maximum resonant power tracking," in

2021 IEEE Custom Integrated Circuits Conference (CICC), 2021, pp. 1–2. DOI: 10.1109/CICC51472.2021.9431456.

[61] S. Sriram, S. Avlani, M. Ward, and S. Sen, "Electro-quasistatic animal body communication for untethered rodent biopotential recording," *Scientific Reports*, vol. 11, no. 1, pp. 2045–2322, 2021. DOI: 10.1038/s41598-021-81108-8.

[62] M. Nath, S. Maity, S. Avlani, S. Weigand, and S. Sen, "Inter-body coupling in electro-quasistatic human body communication: Theory and analysis of security and interference properties," *Scientific Reports*, vol. 11, no. 1, pp. 2045–2322, 2021. DOI: 10.1038/s41598-020-79788-9.

[63] D. Banerjee, S. K. Devarakond, X. Wang, S. Sen, and A. Chatterjee, "Real-time use-aware adaptive rf transceiver systems for energy efficiency under ber constraints," *IEEE Transactions on Computer-Aided Design of Integrated Circuits and Systems*, vol. 34, no. 8, pp. 1209–1222, 2015. DOI: 10.1109/TCAD.2015.2419617.

[64] S. Sen, V. Natarajan, S. Devarakond, and A. Chatterjee, "Process-variation tolerant channel-adaptive virtually zero-margin low-power wireless receiver systems," *IEEE Transactions on Computer-Aided Design of Integrated Circuits and Systems*, vol. 33, no. 12, pp. 1764–1777, 2014. DOI: 10.1109/TCAD.2014.2358535.

[65] S. Sen, D. Banerjee, M. Verhelst, and A. Chatterjee, "A power-scalable channel-adaptive wireless receiver based on built-in orthogonally tunable lna," *IEEE Transactions on Circuits and Systems I: Regular Papers*, vol. 59, no. 5, pp. 946–957, 2012. DOI: 10.1109/TCSI.2012.2191314.

[66] N. Cao, S. Sen, and A. Raychowdhury, "Collaborative intelligence in optical/ir camera based wireless sensor nodes for hvac control," in *2017 IEEE SENSORS*, 2017, pp. 1–3. DOI: 10.1109/ICSENS.2017.8234091.

[67] N. Cao, S. B. Nasir, S. Sen, and A. Raychowdhury, "In-sensor analytics and energy-aware self-optimization in a wireless sensor node," in *2017 IEEE MTT-S International Microwave Symposium (IMS)*, 2017, pp. 200–203. DOI: 10.1109/MWSYM.2017.8059047.

[68] N. Cao, B. Chatterjee, M. Gong, M. Chang, S. Sen, and A. Raychowdhury, "A 65nm image processing soc supporting multiple dnn models and real-time computation-communication trade-off via actor-critical neuro-controller," in *2020 IEEE Symposium on VLSI Circuits*, 2020, pp. 1–2. DOI: 10.1109/VLSICircuits18222.2020.9162878.

[69] N. Cao, S. B. Nasir, S. Sen, and A. Raychowdhury, "Self-optimizing iot wireless video sensor node with in-situ data analytics and context-driven energy-aware real-time adaptation," *IEEE Transactions on Circuits and Systems I: Regular Papers*, vol. 64, no. 9, pp. 2470–2480, 2017. DOI: 10.1109/TCSI.2017.2716358.

[70] B. Chatterjee, N. Cao, A. Raychowdhury, and S. Sen, "Context-aware intelligence in resource-constrained iot nodes: Opportunities and challenges," *IEEE Design Test*, vol. 36, no. 2, pp. 7–40, 2019. DOI: 10.1109/MDAT.2019.2899334.

[71] S. Sen, M. Verhelst, and A. Chatterjee, "Orthogonally tunable inductorless rf lna for adaptive wireless systems," in *2011 IEEE International Symposium of Circuits and Systems (ISCAS)*, 2011, pp. 285–288. DOI: 10.1109/ISCAS.2011.5937557.

[72] D. Banerjee, S. Sen, A. Banerjee, and A. Chatterjee, "Low-power adaptive rf system design using real-time fuzzy noise-distortion control," in *Proceedings of the 2012 ACM/IEEE International Symposium on Low Power Electronics and Design*, ser. ISLPED '12, Redondo Beach, California, USA: Association for Computing Machinery, 2012, pp. 249–254, ISBN: 9781450312493. DOI: 10.1145/2333660.2333719. [Online]. Available: https://doi.org/10.1145/2333660.2333719.

[73] D. Banerjee, B. Muldrey, X. Wang, S. Sen, and A. Chatterjee, "Self-learning rf receiver systems: Process aware real-time adaptation to channel conditions for low power operation," *IEEE Transactions on Circuits and Systems I: Regular Papers*, vol. 64, no. 1, pp. 195–207, 2017. DOI: 10.1109/TCSI.2016.2608962.

[74] S. Sen, "Invited: Context-aware energy-efficient communication for iot sensor nodes," in *2016 53nd ACM/EDAC/IEEE Design Automation Conference (DAC)*, 2016, pp. 1–6. DOI: 10.1145/2897937.2905005.

[75] S. Sen, V. Natarajan, R. Senguttuvan, and A. Chatterjee, "Pro-vizor: Process tunable virtually zero margin low power adaptive rf for wireless systems," in *2008 45th ACM/IEEE Design Automation Conference*, 2008, pp. 492–497. DOI: 10.1145/1391469.1391595.

[76] R. Senguttuvan, S. Sen, and A. Chatterjee, "Vizor: Virtually zero margin adaptive rf for ultra low power wireless communication," in *2007 25th International Conference on Computer Design*, 2007, pp. 580–586. DOI: 10.1109/ICCD.2007.4601956.